Chinese Chemical Letters 37 (2026) 111628

Contents lists available at ScienceDirect

Chinese Chemical Letters

journal homepage: www.elsevier.com/locate/cclet

Current trends in advanced imaging modalities for the early diagnosis of Alzheimer's disease

Xingli Zhang [a], Peng Xue [a,b,*]

[a] School of Materials and Energy, Southwest University, Chongqing 400715, China
[b] Yibin Academy of Southwest University, Yibin 644005, China

ARTICLE INFO

Article history:
Received 2 April 2025
Revised 26 June 2025
Accepted 22 July 2025
Available online 24 July 2025

Keywords:
Alzheimer's disease
Imaging technologies
Nanotechnology
Diagnosis
Theranostics

ABSTRACT

Alzheimer's disease (AD) is a progressive neurodegenerative disorder characterized by complex pathological features such as amyloid-β plaques and tau tangles. Early and accurate diagnosis is crucial for effective intervention, yet remains challenging. This review focuses on current and emerging imaging modalities used in AD detection, including positron emission tomography, single-photon emission computed tomography, magnetic resonance imaging (MRI), fluorescence imaging, photoacoustic imaging, and mass spectrometry imaging, with an emphasis on their mechanisms, advantages, and limitations. Special attention is given to the integration of nanotechnology with imaging platforms, highlighting how nanomaterials enhance diagnostic specificity, sensitivity, stability and therapeutic potential. The review also explores recent advances in multimodal imaging, artificial intelligence-assisted diagnostics, and future directions toward personalized and other non-invasive strategies for early AD diagnosis.

© 2025 Published by Elsevier B.V. on behalf of Chinese Chemical Society and Institute of Materia Medica, Chinese Academy of Medical Sciences.

1. Introduction

In aging societies, Alzheimer's disease (AD) represents a devastating neurodegenerative condition, accounting for 60%–80% of all dementias [1–4]. Furthermore, it is estimated that the global number of individuals with AD will reach 60 million by 2030 [5–7]. Consequently, predicting the potential incidence of AD is critical for monitoring disease progression and guiding personalized pharmacological treatment strategies. Recent studies have shown that the risk of progression from mild cognitive impairment (MCI) to AD increases with the duration of MCI. MCI is categorized into two types: amnestic MCI (aMCI) and non-amnestic MCI (naMCI). While patients with MCI experience varying degrees of memory loss, these symptoms do not meet the established clinical diagnostic criteria for AD. Therefore, MCI is regarded as a transitional phase between normal aging and AD [8–11]. AD is generally classified into two forms: familial AD (FAD) and sporadic AD (SAD). The majority of AD cases (~95%) are sporadic and not genetically inherited. In contrast, familial AD (~5%) results from inherited mutations in specific genes. FAD is commonly associated with mutations in genes encoding amyloid precursor protein (APP), presenilin-1 (PS1), presenilin-2 (PS2), or apolipoprotein E (APOE). While sporadic AD is often age-related, it typically manifests after the age of 65 [12–15].

The primary pathological hallmark of AD is the formation of insoluble neuritic plaques in the cerebral cortex, composed of amyloid-β (Aβ) peptides, as well as neurofibrillary tangles (NFTs) formed by hyperphosphorylated tau proteins [16–18]. Over recent decades, various risk factors, including age [19], gender [20], acetylcholine levels [21], reactive oxygen species (ROS) levels [22], mitochondrial dysfunction [23], and the accumulation of certain metal ions, have been identified as contributing to the development of AD [24]. In the realm of drug development, current clinical trials primarily focus on the amyloid cascade hypothesis and neurotransmitter systems [25]. However, the pre-pathogenic mechanisms underlying AD remain poorly understood [25,26]. Despite extensive efforts, nearly all proposed therapeutic strategies for AD have failed to produce significant clinical outcomes [27]. Existing treatments are largely limited to three acetylcholinesterase (AChE) inhibitors (donepezil, rivastigmine, and galantamine) and a single *N*-methyl-D-aspartate receptor antagonist (memantine). These drugs provide only short-term symptomatic relief, with minimal impact on the disease's progression. Notably, since the approval of memantine by the U.S. Food and Drug Administration (FDA) in 2003, subsequent drugs have failed in clinical trials, demonstrating poor efficacy and unfavorable cost-effectiveness ratios [28]. As a result, drug development for AD has proven to be exceptionally challenging. Current treatments can manage symptoms but are incapable of curing the disease or halting its progression. Thus, early

* Corresponding author at: School of Materials and Energy, Southwest University, Chongqing 400715, China.
E-mail address: xuepeng@swu.edu.cn (P. Xue).

https://doi.org/10.1016/j.cclet.2025.111628
1001-8417/© 2025 Published by Elsevier B.V. on behalf of Chinese Chemical Society and Institute of Materia Medica, Chinese Academy of Medical Sciences.

detection and intervention are critical for reducing the risk of AD. The development of cost-effective, efficient, rapid, and sensitive diagnostic technologies is therefore essential for enabling early-stage detection and improving patient outcomes.

Currently, biomarkers in plasma and cerebrospinal fluid (CSF) are predominantly used for the prediction of AD. Although plasma or CSF testing can provide preliminary insights into neurological disorders, an accurate diagnosis often requires brain biopsy, which is challenging for early-stage AD detection. Cognitive function tests are crucial for assessing cognitive impairments but cannot definitively diagnose dementia or AD [18]. Existing neuroimaging technologies are typically expensive and associated with certain health risks, making them unsuitable for routine AD screening. Notably, brain lesions in AD patients begin to develop approximately 20 years before clinical dementia symptoms emerge. However, current imaging tools can only provide accurate diagnoses in the middle or late stages of AD, by which time irreversible brain damage has already occurred [29]. For instance, diffuse plaques, which do not yet form NFTs, may evolve into insoluble plaques and lead to progressive neuronal atrophy over the next two decades. Unfortunately, these diffuse plaques cannot be detected with current diagnostic techniques. Several imaging modalities, including magnetic resonance imaging (MRI), emission computed tomography (ECT), and photoacoustic (PA) imaging, are commonly used to study the pathological features of AD, monitor therapeutic effects, and evaluate drug efficacy both *in vitro* and *in vivo*. Positron emission tomography (PET) imaging remains the only non-invasive clinical method capable of quantifying cortical Aβ accumulation and propagation in the brains of AD patients. However, PET is a costly modality and is not widely accessible for large-scale public use [9,30]. Thus, there is a critical need for the development of advanced imaging techniques, supported by high-performance contrast agents or tracers, for the early detection of AD. Such technologies would facilitate early intervention and improve the management of patients with early-onset AD (EOAD).

2. Pathological features of AD

2.1. Amyloid

Extracellular deposition of Aβ peptides is a hallmark of AD. According to the amyloid hypothesis, AD results from an imbalance between Aβ production and clearance, leading to plaque formation [31]. Aβ peptides, primarily Aβ40 and the more aggregation-prone Aβ42, are generated by sequential cleavage of APP by β-secretase (BACE1) and γ-secretase [32–34]. These oligomers disrupt synaptic function, form membrane channels permitting Ca^{2+} influx, and initiate inflammatory responses by activating pattern recognition receptors (PRRs) [35]. Structural transition from α-helix to β-sheet conformations contributes to neuronal toxicity. Mutations in APP and secretase cleavage sites increase Aβ42 levels and alter Aβ42/Aβ40 ratios, correlating with disease severity [36,37]. Aβ accumulates as diffuse and focal plaques, often surrounded by activated astrocytes, microglia, and damaged neurons. Cerebral amyloid angiopathy (CAA), present in ~80% of AD patients, involves Aβ40 deposition in vessel walls, compromising blood-brain barrier (BBB) integrity [38,39]. In contrast, parenchymal plaques are rich in Aβ42. A declining Aβ42/Aβ40 ratio is linked to vascular amyloid predominance. Additionally, advanced glycation end-products (AGEs) enhance Aβ aggregation *via* oxidative stress, further driving neurodegeneration (Fig. S1a in Supporting information) [40,41].

2.2. Tau protein

Tau is a microtubule-associated protein (MAP) essential for microtubule stabilization and axonal transport in neurons. In AD, tau undergoes hyperphosphorylation, leading to its dissociation from microtubules and aggregation into insoluble fibrils that form NFTs [42,43]. Tau is natively unfolded, highly soluble, and exists in six isoforms in the central nervous system (CNS). Under physiological conditions, positively charged microtubule-binding domains prevent aggregation by maintaining tau's soluble conformation. Pathologically, changes in tau's isoelectric point promote phosphorylation and truncation, enhancing its oligomerization and assembly into paired helical filaments (PHFs). These aggregates disrupt synaptic function, induce neurotoxicity, and contribute to cognitive decline [43–48]. Post-translational modifications are key drivers of tau aggregation, though hyperphosphorylation alone is not sufficient to induce insoluble filament formation [45,49]. Notably, Aβ peptides can bind to tau, facilitating its detachment from microtubules and promoting NFT formation [45,50]. Tau pathology propagates through a prion-like mechanism, where extracellular tau aggregates are transmitted *trans*-synaptically, amplifying misfolding across brain regions (Fig. S1b in Supporting information) [42,43].

2.3. Metal ions

Abnormal accumulation of trace metals such as iron (Fe), copper (Cu), zinc (Zn), and aluminum (Al) is closely linked to the progression of AD through the exacerbation of amyloid and tau pathologies [23,47,50,51]. These metals of iron, copper, and zinc are physiologically essential for functions such as neurotransmitter synthesis, enzymatic activity, and synaptic signaling, respectively. However, when their homeostasis is disrupted, they can become neurotoxic and contribute to AD pathology. Elevated iron levels promote lipid peroxidation and oxidative damage, while excess copper facilitates Aβ aggregation and increases oxidative stress. Aluminum contributes to tau hyperphosphorylation and enters the brain *via* both the BBB and the olfactory route, further accelerating neurotoxicity and cognitive decline. Zinc imbalance disrupts synaptic homeostasis and may activate NLRP3-mediated neuroinflammation [24,47]. Fe^{3+}, Cu^{2+}, and Zn^{2+} have been found enriched in Aβ plaques, NFTs, and synaptic regions of AD brains [52]. These metals form complexes with Aβ (*e.g.*, Cu(II)-Aβ, Fe(III)-Aβ, Zn(II)-Aβ), enhancing Aβ oligomerization and generating cytotoxic partially reduced oxygen species (PROS) that activate microglia and drive chronic inflammation [4,53–55]. Additionally, Aβ-heme complexes exhibit elevated peroxidase-like activity, further contributing to oxidative neuronal damage (Fig. S1c in Supporting information).

2.4. Other pathogenic mechanisms

Beyond amyloid and tau pathology, several interconnected mechanisms contribute to AD progression. Neurotransmitter dysregulation plays a pivotal role, with early impairments in glutamate uptake leading to excitotoxicity and sleep disturbances [56–58]. Dysfunction of metabotropic glutamate receptors, particularly mGluR5, disrupts calcium homeostasis and synaptic integrity through Aβ-induced aggregation [59,60]. Dopaminergic and cholinergic deficits, marked by altered dopamine signaling and increased AChE and butyrylcholinesterase (BChE) activity, are closely associated with cognitive decline [61,62]. Metabolic dysfunctions also contribute significantly. Elevated methylglyoxal (MG), a precursor of advanced AGEs, induces oxidative stress and neuronal death, especially when detoxification by the glyoxalase pathway is impaired [41,63,64]. Mitochondrial dysfunction through reduced adenosine triphosphate (ATP) production and proapoptotic factor release further accelerates neuronal loss [65–67]. Other contributors include formaldehyde toxicity, glucose and polyunsaturated fatty acid metabolic disruption, oxidative stress, and altered nitric oxide (NO) signaling [55,68–70]. These multifactorial processes in-

teract to exacerbate neurodegeneration and cognitive impairment in AD (Fig. S1d in Supporting information).

3. Imaging modalities for AD diagnosis

While significant progress has been made in understanding the pathological features of AD, numerous challenges remain in the early diagnosis and subsequent management of the disease. Several neuroimaging techniques play a crucial role in the diagnosis and investigation of AD. Notably, MRI, ECT, PA imaging, ultrasound (US) imaging, fluorescence imaging, spectroscopic imaging, and multimodal imaging are of paramount importance in the detection of AD. The following sections will discuss the recent advancements in these imaging modalities for the diagnosis of AD.

3.1. MRI

MRI is based on the principles of nuclear magnetic resonance (NMR), wherein atomic nuclei, particularly hydrogen protons, absorb and emit radiofrequency (RF) energy when subjected to an external magnetic field. These nuclei subsequently return to their equilibrium state through relaxation processes, during which they emit RF signals that are used to generate images [71]. MRI is non-invasive and does not require the use of radioactive tracers. It provides high spatial resolution images of anatomical brain structures and offers excellent soft-tissue contrast with remarkable sensitivity [72,73]. Additionally, MRI is one of the most cost-effective and widely accessible imaging modalities [74]. MRI scans can aid in detecting abnormalities in the brain, helping to assess the risk of AD development or the progression of existing AD [75]. MRI techniques are rapidly advancing and can be categorized into functional MRI (fMRI), structural MRI (sMRI), and arterial spin-labeled MRI (ASL-MRI), each of which provides distinct information regarding the body's tissues [76–78].

3.1.1. fMRI

fMRI, particularly blood-oxygenation-level-dependent (BOLD) imaging, has been pivotal in cognitive neuroscience [9,79]. It detects neural activity by measuring hemodynamic changes related to blood oxygenation, enabling visualization of brain responses to various stimuli [79–81]. Ren *et al.* used resting-state fMRI to assess multiscale entropy (MSE) in healthy, AD, and aMCI groups, identifying time-scale-dependent correlations between MSE changes and cognitive deficits, which suggests MSE as a potential AD biomarker (Fig. 1a) [82]. Combining graph convolutional networks (GCNs) with random forests, researchers used functional connectivity (FC) data from resting-state fMRI to indirectly predict Aβ-PET findings [83]. Additionally, fMRI studies of the locus coeruleus (LC) revealed greater degeneration in EOAD than in late-onset AD (LOAD), which proposes a potential biomarker for disease differentiation [84]. Real-time fMRI (rtfMRI) with neurofeedback may also help detect early neuroplastic changes linked to cognitive decline [85].

Magnetic resonance spectroscopy (MRS), especially proton MRS (^{1}H-MRS), complements fMRI by providing neurochemical insights [71]. Since 2014, it has been widely used to monitor metabolites like *N*-acetyl-aspartate and inositol, aiding in the prediction of AD progression from MCI [86–88]. Chemical exchange saturation transfer (CEST) imaging offers molecular-level analysis of substances like glucose and glutamate. CEST-MRI using the angiopep-2 (ANG) biomarker has shown high specificity and sensitivity for *in vivo* Aβ detection (Fig. 1b) [89]. Accurate CEST quantification requires minimizing interference from water saturation and magnetization transfer contrast [74,87,88]. Magnetic nanoparticles significantly enhance MRI sensitivity and specificity [90]. Gadolinium-based agents detect amyloid plaques as small as 36 μm, while superparamagnetic iron oxide nanoparticles (SPIONs) enable efficient

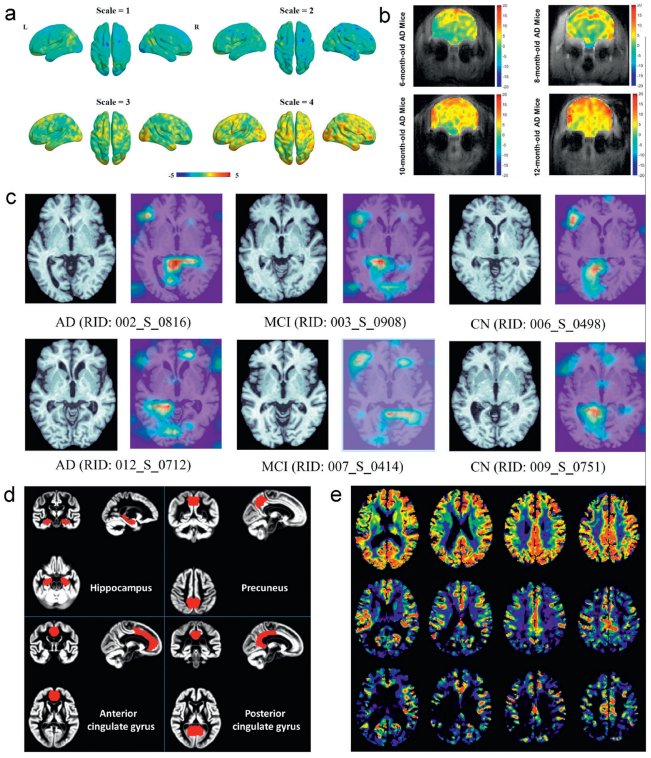


Fig. 1. Different MRI modes for early AD diagnosis. (a) The comparison of MSE patterns between AD and health control in different time scales based on resting-state BOLD signals (scale 1 and 3: AD; scales 2 and 4: HC). Reproduced with permission [82]. Copyright 2020, Rapamycin Press LLC. (b) CEST-MRI images of 6-, 8-, 10-, and 12-month-old AD mice during 60 min following ANG injection. Reproduced with permission [89]. Copyright 2023, American Chemical Society. (c) Grad-CAM visualization. Red (large) and purple (small) indicate the effects on the model. Reproduced with permission [104]. Copyright 2023, Elsevier B.V. (d) DWI images of voxel-of-interest (VOI) templates in terms of bilateral hippocampi, precunei, and the anterior and posterior cingulate gyri. Reproduced with permission [75]. Copyright 2017, Elsevier Ltd. (e) Quantitative CBF mapping measured by ASL-MRI. Blank control, aMCI and AD groups are assigned to the photos in the top, middle and bottom rows, respectively. Reproduced with permission [109]. Copyright 2023, SciELO.

AD-related tissue assessment through uptake by the reticuloendothelial system [72,73,91,92].

3.1.2. sMRI

sMRI differs from fMRI by focusing on detecting brain lesions, injuries, and abnormalities, such as atrophy in attention-deficit/hyperactivity disorder (ADHD) and neurodegenerative diseases like AD [93]. For example, sMRI is used to identify atrophy in the parietal and posterior temporal cortex in sporadic EOAD. Rubinski *et al.* utilized sMRI to distinguish between brain tissue types like gray matter, white matter, and CSF [94–96]. Advances in deep learning, such as the 3D attention network (3DAN), enhance AD diagnosis by extracting imaging biomarkers with improved accuracy [97]. Similarly, the learning vector quantization-support vector machine (LVQ-SVM) algorithm has achieved high classification accuracy in distinguishing healthy individuals from AD patients [98].

Several other models, including the SSFSHHO-FKNN framework, AutoLoc, and BrainStatTrans-GAN, have been integrated with sMRI to classify AD and predict progression from MCI to AD [99]. AutoLoc achieved 93.38% accuracy in AD classification, while BrainStatTrans-GAN demonstrated 90.4% accuracy for AD and 78.7% for MCI [100–103]. Furthermore, the PMDA framework, which incorporates multi-scale feature extraction, reached impressive classification accuracies for AD *vs.* cognitively normal (CN) and AD *vs.* MCI (Fig. 1c) [104]. Diffusion tensor imaging (DTI), an advanced structural imaging technique, measures the diffusion of wa-

ter molecules in brain tissue to evaluate the integrity of axons within white matter tracts [105]. When combined with sMRI, DTI enhances AD classification reliability. Diffusion-weighted imaging (DWI) further aids in tracing white matter fascicles and calculating volumes and diffusion coefficients of key brain regions (Fig. 1d). Topological alterations in white matter connectivity are linked to cognitive performance and could serve as early biomarkers for AD. Shu *et al.* demonstrated that disruptions in structural connectivity are evident in patients with multidomain aMCI, highlighting neurobiological changes underlying cognitive impairment [106].

3.1.3. Others

ASL-MRI relies on the contrast provided by inflowing, electromagnetically labeled blood, eliminating the need for exogenous contrast agents. This enables the measurement of cerebral perfusion and structural features at the tissue level [78,107–109]. Cerebral blood flow (CBF) is a critical biomarker for the early diagnosis of AD [109]. For instance, global perfusion reductions and regional hypoperfusion are commonly observed in the brains of patients with aMCI and AD, and these changes can be detected using ASL-MRI techniques [78]. Further studies utilizing ASL-MRI have measured CBF across individuals of different ages, revealing a statistical correlation between age and CBF [110]. The combination of hippocampal volumetry and CBF measurements from ASL-MRI provides higher accuracy in differentiating AD patients from cognitively normal elderly adults [107]. In addition, voxel-based morphometry (VBM) procedures applied to normalized CBF measurements from ASL-MRI offer improved morphological analysis in AD discrimination (Fig. 1e) [111].

Innovations such as DTI, ASL, and fMRI have provided deeper insights into microstructural changes, cerebral perfusion, and neuronal activity in early-stage AD. Of particular interest is the emergence of quantitative susceptibility mapping (QSM) and magnetization transfer imaging (MTI), which allow for the non-invasive assessment of iron deposition and myelin integrity, respectively. Additionally, molecular MRI using targeted contrast agents (*e.g.*, Aβ-specific gadolinium chelates or SPIONs) is under active investigation to achieve disease-specific imaging. Currently, Gd-based contrast agents are among the most widely approved and clinically used agents for MRI, though concerns regarding nephrogenic systemic fibrosis (NSF) and Gd retention have prompted safety reevaluations. SPIONs have shown promising results in preclinical and early clinical studies due to their high magnetic susceptibility and efficient uptake by the reticuloendothelial system. Imaging agents such as angiopep-2-modified probes used in CEST-MRI are undergoing clinical validation for enhanced BBB penetration and targeted Aβ plaque detection. Despite these advances, challenges persist, including variability in BBB permeability, off-target effects, and inconsistent contrast enhancement, which may limit their widespread adoption.

3.2. ECT

Single photon emission computed tomography (SPECT) and PET are well-established imaging techniques used for the diagnosis of neurodegenerative disorders such as MCI and AD. These modalities involve the use of positron-emitting or single-electron radioisotopes that are covalently conjugated to targeting reagents for non-invasive imaging of Aβ plaques and tau proteins in the brain. Each radioisotope, or radionuclide, undergoes a unique radioactive decay process. For instance, the commonly used radioisotopes for high-resolution PET imaging include ^{11}C, ^{18}F, and ^{64}Cu, with half-lives of 20 min, 110 min, and 12.7 h, respectively [112–114]. In contrast, radioisotopes typically used in SPECT imaging include iodine-123 (^{123}I), technetium-99 m (^{99m}Tc), xenon-133 (^{133}Xe), thallium-201 (^{201}Tl), and fluorine-18 (^{18}F). One important physicochemical parameter that influences the pharmacokinetics of these radioisotopes is lipophilicity, which is related to the clearance rate and half-life of the tracer. ^{18}F-labeled probes generally exhibit lower lipophilicity compared to ^{123}I-labeled probes, which may explain the superior spatial resolution, signal attenuation, and imaging sensitivity of PET over SPECT [115–117]. Fluorescent dyes, such as Congo red, thioflavin-S (ThS), and thioflavin-T (ThT), are commonly employed as histological tools to visualize senile plaques and NFTs associated with AD. Therefore, SPECT and PET imaging modalities offer the added advantage of being able to diagnose and differentiate AD from other forms of dementia.

3.2.1. PET

AD is characterized by the progressive accumulation of Aβ plaques and tau tangles [118]. PET is a powerful imaging tool for visualizing and quantifying these pathological changes. Radiotracers like [^{11}C]PiB and [^{18}F]florbetapir can detect Aβ plaques 10–20 years before clinical symptoms appear [119]. [^{11}C]PiB has high affinity for both Aβ1–40 and Aβ1–42 peptides and shows specific uptake in telencephalic regions containing Aβ plaques, enhancing its sensitivity for AD detection. Other Aβ imaging agents, such as [^{18}F]BIBD-124/127, show favorable pharmacokinetics and reduced defluorination, making them promising candidates for clinical trials (Fig. S2a in Supporting information) [120,121]. Currently, [^{18}F]AV45, [^{18}F]FPiB, and [^{18}F]AV1 are commercially available PET probes for Aβ imaging. Tau imaging, however, is less developed [122]. The [^{18}F]FDDNP probe binds both tau tangles and Aβ plaques, while other tracers like [^{18}F]PI-2620, [^{18}F]T807, and [^{18}F]flortaucipir are specifically designed to image tau pathology in AD [118,122–124]. However, first-generation tau tracers suffer from off-target binding, limiting their diagnostic accuracy for AD. Second-generation tracers, such as [^{18}F]MK-6240 and [^{18}F]JNJ64349311, show promise for better specificity and reduced off-target binding [118,119,122–124]. [^{18}F]RO-948, for instance, has shown high affinity for tau aggregates in AD brains, with lower reactivity in non-AD tauopathies [125,126]. Moreover, tau PET has revealed that atypical AD forms show higher tau burden in the cerebral cortex compared to typical AD [125].

Fluorodeoxyglucose (FDG)-PET is another promising modality for detecting early brain changes in AD and pre-dementia stages like aMCI. ^{18}F-FDG, a radiolabeled glucose analog, visualizes glucose metabolism in the brain, providing insights into neuronal activity and metabolic dysfunction [127,128]. FDG-PET has been shown to detect hypometabolism in key brain regions, offering superior accuracy over MRI for diagnosing aMCI (Figs. S2b and c) [94,128,129]. PET ligands based on antibodies, such as [^{125}I]8D3-F(ab')2-h158, have shown potential for early AD diagnosis, with higher concentrations in cortical regions compared to [^{11}C]PiB [130]. Additionally, radiolabeled antibody-based ligands like [^{124}I]RmAb158-scfv8D3 have been developed to detect Aβ in early AD diagnosis [130,131]. PET imaging also highlights the role of P-glycoprotein (P-gp) in Aβ clearance [132]. Decreased P-gp levels are associated with impaired Aβ clearance in AD patients. Copper(II)-based PET tracers, with thiosemicarbazone-pyridylhydrazone ligands, have been synthesized for Aβ plaque imaging with high specificity [133]. Finally, while PET shows a linear correlation with AD progression, it is limited in predicting the conversion from aMCI to AD. Combining PET with sMRI and MRS could provide more comprehensive insights into disease progression, improving the accuracy of conversion timelines and aiding in disease staging [134].

3.2.2. SPECT

While the spatial resolution and quantitative accuracy of SPECT are generally lower than PET, SPECT remains crucial for AD di-

agnosis [114,116]. [^{123}I]IMPY is one of the SPECT probes used for Aβ imaging but suffers from weak signal strength, highlighting the need for more effective radiotracers [135]. Technetium-99 m (^{99m}Tc) is a commonly used radionuclide in SPECT due to its favorable properties [136,137]. Several ^{99m}Tc derivatives, such as [^{99m}Tc]5 and [^{99m}Tc]14b, have been developed for Aβ plaque imaging, but they face challenges with cerebral penetration, limiting their clinical utility [135–139].

Protein-based SPECT probes for Aβ detection are hindered by poor BBB penetration and enzymatic degradation [38]. [^{123}I]ABC577, a triazole-substituted derivative, shows high affinity for Aβ plaques but suffers from non-specific cortical uptake, which affects diagnostic accuracy [114,140]. [^{123}I]IMPY also demonstrates similar limitations [112,136,138]. ^{99m}Tc remains the preferred agent for SPECT Aβ imaging, with the ^{99m}Tc1–3 complex showing the highest cerebral uptake reported for SPECT, offering potential for both diagnostic and therapeutic applications [138,139]. Recent advancements include [^{125}I]PIP-NHMe, a novel SPECT probe for tau imaging, which exhibits rapid clearance and high selectivity. Additionally, antibody-based probes like TCO- [^{125}I]I-RmAb158 have shown improved imaging contrast in AD models, indicating enhanced clearance and earlier detection opportunities [141,142].

Dual-modality imaging techniques, which combine SPECT with other modalities, offer enhanced sensitivity and specificity. For instance, regional CBF (rCBF) SPECT has been shown to predict amyloid pathology patterns in both typical and atypical AD [143]. SPECT-EEG integration improves diagnostic accuracy for cognitive impairments, while deep learning models applied to Tc-99m-ECD SPECT can differentiate AD from Lewy body dementia (LBD) [144,145]. Furthermore, [^{123}I]FP-CIT SPECT is highly accurate in distinguishing AD from other forms of dementia, such as Parkinson's disease (PD) and dementia with Lewy bodies (DLB), achieving 94% accuracy for differentiating AD from DLB [146]. Despite its advantages, CT is rarely combined with SPECT in clinical practice due to its lower spatial resolution and the need for large, specialized equipment [147]. Overall, while many imaging agents have demonstrated acceptable safety profiles in clinical settings, ongoing development is required to optimize pharmacokinetics, minimize off-target effects, and improve diagnostic accuracy, especially for tau imaging and in resource-limited environments.

3.3. US imaging

Unlike CT scans, US imaging carries no radiation risk and provides high anatomical resolution, enabling precise imaging of deep structures such as capillaries [148–151]. Focused US (FUS) has recently gained attention as a promising tool for *in situ* photon emission and neuromodulation. When combined with circulating microbubbles, FUS is currently the only non-invasive, transient, and reversible method to open the BBB with high precision. As such, FUS-based strategies show considerable potential for both diagnosing and treating AD. For example, Wang *et al.* developed liposomal nanoparticles (Lipo@IR780/L012) for FUS-triggered mechanoluminescence in the brain, enabling non-invasive optogenetic manipulation with high temporal resolution and favorable biocompatibility [152,153]. Notably, the combination of proteolytically degradable nanoscale contrast agents with quantitative US imaging offers the possibility of non-invasive, functional imaging of cellular degradative processes in the cerebral neurons of AD patients [154].

US imaging offers a cost-effective alternative, enabling visualization of tissue structures on planar surfaces and the measurement of CBF based on the Doppler effect [149]. Functional US (fUS) enables non-invasive imaging of neurovascular alterations, bypassing cranial restrictions, and can provide valuable insights into cerebral hemodynamics. For instance, the retinal hemodynamic response function can be characterized *in vivo* following visual stimuli, making the retina an accessible window into the nervous system (Fig. S2d in Supporting information). Alterations in neurovascular coupling may occur during the pathogenesis of AD, and retinal hemodynamics have been linked to the progression of neurodegenerative disorders [151]. Lassila *et al.* demonstrated that carotid ultrasonography could improve the diagnostic accuracy for dementia and AD by measuring ambulatory blood pressure. Transcranial Doppler US measurements, including assessments of decreased CBF and increased pulse index, have been shown to be linked to the development of aMCI [149]. In addition, high-spatiotemporal-resolution vector micro-Doppler imaging (HVμDI) based on contrast-free, ultrafast, high-frequency US imaging can visualize cerebrovascular hemodynamics in mice with high sensitivity (Fig. S2e in Supporting information) [155]. HVμDI holds promise for diagnosing AD by not only imaging CBF but also quantifying cortical and hippocampal vessel density [156].

Commonly used US contrast agents include microbubble-based formulations such as Definity®, Lumason® (SonoVue®), and Optison®, which are composed of gas-filled lipid or protein shells. These agents are FDA-approved for enhancing vascular imaging due to their excellent echogenicity, high safety profile, and short systemic half-life. They are primarily used to improve delineation of vascular structures, assess perfusion, and detect abnormal flow patterns, which is particularly relevant in the context of AD where cerebral perfusion deficits are key features. Emerging nanoscale agents, including phase-change nanodroplets and engineered protein nanostructures, offer enhanced stability, deeper tissue penetration, and potential for molecular targeting. However, challenges such as immune clearance, limited BBB permeability, and regulatory concerns about long-term safety and biodegradability remain. Furthermore, while most clinical agents are approved for cardiovascular or hepatic imaging, their application in neuroimaging is still under investigation.

3.4. PA imaging

By integrating the high contrast of light and the deep penetration capabilities of standard US, PA imaging enables precise localization and non-invasive physiological and pathological imaging. PA imaging does not rely on ionizing radiation, which makes it a safer alternative to techniques such as CT and other X-ray-based methods [157–160]. For instance, the elevated concentration of Cu^{2+} ions in the brain has been implicated in the accumulation of pathological Aβ, a hallmark of AD. Traditional detection strategies face challenges in offering non-invasive and accurate Cu^{2+} quantification in deep tissues. A novel PA nanoprobe, NRh-IR-NMs, was developed for ratiometric PA imaging of Cu^{2+} with high selectivity and tissue penetration depth. This probe incorporates a Cu^{2+}-responsive probe (NRh) as the indicator and a nonresponsive dye as an internal reference (Fig. S3a in Supporting information) [160]. In another approach, ultrathin zinc selenide (ZnSe) nanoplatelets were engineered as PA probes to monitor brain Cu^{2+} levels [161]. Highly sensitive imaging of NO in the brain is crucial for understanding the pathophysiological processes underlying neurodegenerative diseases. PANO1–3 PA probes were developed to visualize the distribution of NO in the mouse brain at micron resolution, offering the potential for PA probes with BBB-crossing capability for studying neurodegeneration [162]. Homogeneous-resolution arched-scanning PA microscopy (AS-PAM) has emerged as a powerful tool for quantitatively imaging the vascular features of the meninges and cortex (Fig. S3b in Supporting information) [163].

PA computed tomography (PACT) leverages the PA effect to generate high-resolution images with deep tissue penetration and enhanced contrast. For example, ratiometric PACT imaging probes such as APC-1 and APCT have been developed for Cu(II) detection. These PA probes incorporate an aza-BODIPY dye scaffold, which

exhibits dual-wavelength near-infrared (NIR) absorbance bands. The combination of a unique dual-wavelength absorbance profile and the low apparent p*K*a of the dichlorophenol group results in a substantial turn-on response (100.5-fold) in the presence of Cu(II) [158,164]. PACT obviates the need for magnetic fields, enabling the quantification of oxygen saturation and blood volume by measuring concentrations of deoxyhemoglobin and oxyhemoglobin. Functional PACT demonstrates a strong spatial correspondence and temporal correlation between CBF and PA signals, allowing for efficient imaging of the human cerebral vascular system and enabling rapid detection of functional activation (Fig. S3c in Supporting information) [165]. Furthermore, PACT has been used to monitor hyperoxia- and hypoxia-induced changes in cerebral hemodynamics, offering insights into brain function [166].

Multispectral photoacoustic tomography (MSOT) utilizes multi-wavelength excitation to spectroscopically analyze the chemical composition of endogenous molecules or contrast agents, providing additional information that is not readily obtainable through other imaging techniques [147,167]. Curcumin-derived CRANAD-2 is a suitable contrast agent for MSOT imaging of Aβ deposits in mouse models of AD cerebral amyloidosis (Fig. S3d in Supporting information) [147]. In addition, polymer-coated gold nanorods (GNRs) have been employed as MSOT contrast agents by conjugating them with anti-Aβ antibodies, which are then attached to preformed Aβ seeds [167]. Unlike traditional optical imaging modalities, volumetric MSOT (vMSOT) is not limited by photon scattering but is governed by US diffraction. vMSOT, coupled with a NIR oxazine derivative Aβ probe (AOI987), allows for the 3D mapping and quantification of Aβ deposits throughout the entire brain in mouse models of AD [168]. Beyond Aβ detection, vMSOT has also been utilized to visualize tau protein accumulation with a spatial resolution of 115 μm [169]. Thus, vMSOT integrates multiplexing capabilities with real-time 3D imaging, positioning it as a promising technique for the effective diagnosis and exploration of AD [147].

To date, various types of nanoparticles have been developed as PA probes, including inorganic nanoparticles (*e.g.*, gold, iron, molybdenum, and copper-based nanoagents), organic nanoparticles (*e.g.*, ICG-conjugated polymers and mesoionic dye A1094-encapsulated nanocomplexes), and semiconductor nanoparticles (*e.g.*, perylene-3,4,9,10-tetracarboxylic diimide and benzodithiophene/benzobisthiadiazole nanospheres). These diverse nanoparticles contribute to expanding the capabilities of PA imaging modalities [170]. However, for neurodegenerative diseases like AD, no PA imaging agent has yet reached clinical approval, primarily due to challenges in BBB penetration, off-target effects, and regulatory hurdles. Future efforts should focus on designing biocompatible, brain-penetrant, and stimuli-responsive PA probes with high specificity, along with robust clinical validation to facilitate their translation into human studies.

3.5. Fluorescence imaging

While traditional brain imaging techniques such as CT, SPECT, and PET provide whole-body images, the associated ionizing radiation poses a risk of cellular damage and tissue harm. Similarly, spatial resolution in MRI is constrained by the signal detection sensitivity of nuclear magnetic resonance (NMR). NIR fluorescence (NIRF) imaging, by contrast, is a simple, non-invasive, and cost-effective modality that serves as a complementary tool to more expensive imaging techniques (*e.g.*, MRI, PET, and CT) [171–173]. Particularly useful for early AD diagnosis, NIRF imaging offers advantages such as low instrument requirements, rapid data acquisition, minimal photodamage, high sensitivity, and deep tissue penetration. Donor-acceptor NIRF probes, with high affinity for Aβ plaques, are often constructed with conjugated π-electron chains. Probes featuring longer conjugated π systems (carbon-carbon double bonds) typically display optimal emission wavelengths in phosphate-buffered saline (PBS) (>650 nm) [27,174–176]. NIRF dyes, such as methylene blue (MB) and fluorescein isothiocyanate (FITC), have been utilized for preoperative detection and intraoperative visualization of brain tumors [177].

Given that Aβ peptides primarily exist in either soluble or insoluble forms, fluorescent probes such as BAP-1, AOI-987, and DANIR-2c have been developed for the detection of insoluble Aβ aggregates [27,178]. Specifically, a series of D-π-A-based Aβ probes, with PEG modified acceptors, are designed to optimize lipophilicity and improve the pharmacokinetics of NIR probes targeting Aβ plaques. The length of the π bridge has been shown to be a critical factor influencing the emission wavelength, quantum yield, and binding affinity to Aβ aggregates [176]. For instance, DSPE-PEG2000 copolymer is used to encapsulate curcumin, forming micelles *via* the solvent evaporation method, for fluorescence imaging of retinal Aβ plaques to diagnose AD [179]. Other probes, including QD-PEG-BTA, ZT-1, AD-1, 4a1, CPDs, BMAOIs, and PDPP, have been developed for the early detection of Aβ plaques *via* NIRF [27,175,178,180–183]. In contrast to Aβ plaques, hyperphosphorylated tau proteins are the primary components of NFTs, which are strongly associated with the progression and severity of cognitive deficits [184]. Tau-selective, smart NIRF probes have been developed by incorporating a 3,5-dimethoxy-*N*,*N*-dimethylanilin-4-yl moiety core scaffold, combined with the characteristic donor-π-acceptor architecture of NIRF probes, such as DANIR-2c and MCAAD-3 [185].

In addition to tau and Aβ aggregates, other pathological features of AD can also be detected using NIR fluorescence NIRF imaging with reliable probes. For example, zinc oxide nanoclusters (ZnO NCs) can accumulate in the hippocampal region, enabling targeted and rapid *in vivo* fluorescence imaging [55]. A Golgi-targeted NO probe, Golgi-NO, has been developed by incorporating a NO recognition moiety (*o*-diaminobenzene) with a Golgi-localizing fluorophore (Golgi-RhB), facilitating sensitive and selective detection of NO within the Golgi apparatus during AD progression [186]. Additionally, a NIRF probe, Chy-1, has been designed for the specific detection of BChE activity, demonstrating excellent sensitivity and biocompatibility, with a limit of detection (LOD) of 0.12 ng/mL [62].

This increased tissue transparency in the NIR-II region enables more effective imaging of deeper biological tissues. However, NIR-II dyes face challenges in crossing the BBB due to their larger molecular size and increased hydrophobicity [172,177]. To address this, a series of boron difluoride (BF2) formazanate NIR-II dyes have been developed with tunable photophysical properties, excellent photostability, and high biological stability. These dyes, modified with morphine derivatives on the aniline fraction, demonstrate improved BBB penetration, enabling effective *in vivo* NIR-II fluorescence imaging of the brain, including both the epicranium and cranium [172]. Additionally, the high fidelity of AgAuSe quantum dots (QDs) as NIR-II fluorescence probes enables multiscale imaging, from whole-body to single-cell levels, with the added advantage of acetylcholine receptor targeting [187]. A "D-A-D" type NIR-II probe, incorporating *N*,*N*-diethylaniline as the recognition group and a boron difluoride-bridged azafluvene as an electron-withdrawing group, selectively targets Aβ oligomers in the NIR-II biowindow for *in vivo* imaging [188]. Furthermore, various advanced NIRF imaging applications, such as multiphoton fluorescence imaging, fluorescence lifetime imaging, and fluorescence resonance energy transfer (FRET) imaging, are being explored for the early diagnosis of AD.

3.5.1. Multiphoton fluorescence imaging

Multiphoton microscopy, in particular, is currently regarded as the optimal method for imaging deep tissue in living brains or

intact animal specimens due to its several advantages, including NIR excitation and emission, minimal photobleaching and photodamage, reduced interference from autofluorescence, and the ability to generate high spatial resolution 3D images [189]. The penetration depth of multiphoton fluorescence imaging is less constrained by the wavelength of the shorter-wavelength fluorescence light [70,189–192]. Two-photon fluorescence imaging, which uses two red photons to excite a fluorophore typically excited by a single green photon, overcomes the issue of photobleaching and inherently provides 3D resolution due to the intensity-squared dependence of two-photon absorption [191,192]. An iminocoumarin-thiazole (ICT) fluorescence probe, ICTAD-1, has been developed to exhibit distinct spectral characteristics for detecting Aβ40 and Aβ42 fibrils *via* two-photon fluorescence imaging (Fig. S4a in Supporting information) [193]. Another example is the two-photon fluorescent probe NATP, designed to monitor $ONOO^-$ levels in brain tissue [194]. The WAPP-4 probe, which exhibits two-photon NIR emission (920/705 nm), demonstrates a large Stokes shift ($\Delta\lambda = 324$ nm in ethanol) and exceptional BBB permeability, enabling effective characterization of Aβ plaque distribution and morphology in brain sections [195].

Monoamine oxidases (MAOs), crucial enzymes in neurodegeneration, are central to AD pathology. A reaction-based two-photon MAO probe has been developed to monitor both MAO activity and Aβ plaques, relying on its ability to efficiently cross the BBB and provide detailed imaging in deep cerebral regions [192]. Additionally, a two-photon fluorescence imaging probe, combining organic and inorganic components, has been designed to specifically detect NO in neurons and zebrafish brain tissue, making it a promising tool for monitoring NO distribution and concentration in the brains of AD patients [196]. A bifunctional two-photon fluorescent probe, BTNPO, based on an oxindole-functionalized benzothiazole-naphthalene derivative, enables the simultaneous visualization of both Aβ aggregates and $ONOO^-$ [191]. Compared to two-photon fluorescence microscopy, three-photon excitation enables imaging at depths of up to 1.4 mm into the cortical tissue, offering high-resolution images in scattering tissues. This technique has also been applied to visualize Ca^{2+} signaling in astrocytes, demonstrating its potential for advanced *in vivo* neuroimaging [189].

3.5.2. Fluorescence lifetime imaging

In recent years, fluorescence lifetime imaging has emerged as a powerful method for the quantitative detection of tissue and intracellular biomarkers, enhancing its applicability in both basic biological studies and clinical diagnostics [197,198]. Luminescent Ru(II) phenanthroline complexes exhibit long-lived emission in the visible spectrum and serve as reversible inhibitors of AChE and BuChE with high specificity. Using this technique, protofibrils were identified in the self-assembly of Aβ1–40, while globular structures were detected in the shorter fragment Aβ15–21 [199]. Two-photon fluorescence lifetime imaging combined with FRET was used to confirm direct molecular interactions between Aβ and CD14, revealing a molecular interaction on the nanometer scale. This interaction highlights the role of the lipopolysaccharide (LPS) receptor CD14 in the pathophysiology of AD [200]. A novel two-photon fluorescence lifetime imaging probe (TFP) was developed to quantify mitochondrial hydrogen peroxide (H_2O_2) and ATP levels in neurons. The TFP probe reveals the relationship between oxidative stress-induced mitochondrial dysfunction and the alterations in intracellular H_2O_2 and ATP levels during the pathological progression of AD (Fig. S4b in Supporting information) [201]. Astrocytic calcium homeostasis is closely linked to neuronal health and AD pathology. Fluorescence lifetime imaging of resting calcium (Ca^{2+}) levels in astrocytes reveals the occurrence of intercellular calcium waves exclusively in the presence of Aβ plaques in mice [202].

3.5.3. FRET imaging

FRET is a phenomenon wherein energy is transferred from an excited fluorophore to a nearby chromophore, typically within a distance of approximately 10 nm [203,204]. A range of nanoparticles has been employed in FRET assays, including semiconductor QDs, graphene QDs (GQDs), up-conversion nanoparticles (UCNPs), gold nanoparticles (AuNPs), and graphene oxide (GO) [203]. To enable accurate detection of Aβ oligomers, a fluorescent biosensor has been developed by incorporating fluorescein-modified Aβ aptamers as the fluorophore and 3D Fe_3O_4/MXene nanospheres as the fluorescence quencher. The Fe_3O_4/MXene nanosphere-based biosensor demonstrates a robust linear correlation between fluorescence intensity and the logarithmic concentration of Aβ oligomers in the range of 0.10–200 nmol/L [205]. The inner filter effect (IFE) occurs when the absorption of excitation or emission light by an absorber overlaps with the fluorescence spectra of the donor fluorophore in the detection system. A novel, label-free, highly selective, and sensitive method for visualizing Aβ oligomers has been proposed, based on the IFE of AuNPs on the fluorescence of CdTe QDs. In the presence of Aβ oligomers, the aggregation of AuNPs is inhibited, resulting in the quenching of CdTe QD fluorescence [203]. In an alternative approach, H-UCNPs-SiO_2@ZIF-8/BHQ-1 (H-USM/BHQ-1) microspheres are synthesized to enable precise quantification of Aβ oligomers using the 540 nm and 654 nm emission ratios of highly doped UCNPs as reporters [206].

MicroRNA-125b (miR-125b) has been implicated in synaptic dysfunction and tau hyperphosphorylation during the early stages of AD pathogenesis. To facilitate the rapid detection of miR-125b, a dual "turn-on" fluorescence biosensor, TPET-DNA@Dex-MoS_2, has been developed for real-time imaging of AD-associated microRNAs [207]. A self-assembled nanoparticle-mediated amplified fluorogenic immunoassay (SNAFIA) enables analysis of liquid biopsy samples, thereby enhancing clinical trial efficiency and expediting the development of therapeutic interventions for AD [208]. A simple approach involving the coupling of the natural product resveratrol (Res) with graphene oxide (GO) results in the formation of Res@GO composites. Upon interaction with Aβ, the composite emits fluorescence due to the inhibition of energy transfer between GO and photoexcited Res [209].

3.5.4. Others

In recent years, synchrotron-based X-ray fluorescence microscopy (XFM) has emerged as the "gold standard" for determining the distribution of elemental and chemical species in biological tissues at various spatial resolutions. Its spatial resolution is comparable to that of inductively coupled plasma mass spectrometry (ICP-MS), yet XFM offers faster and more reliable sample processing. To explore the relationship between metal content and anatomical Aβ plaque deposition, metal distribution in the hippocampus of APP/PS1 mice has been assessed using XFM. The findings reveal an elevation in zinc (Zn) content in the plaques, which may be associated with the initiation of Aβ production [210]. A multifocal illumination fluorescence microscope is capable of detecting Aβ deposits across the entire brain [211]. The combination of label-free super-resolution spectroscopy for subcellular imaging, based on novel optical photothermal infrared (O-PTIR) and XFM imaging techniques, enables unprecedented resolution of elemental distributions and fibrillary forms of Aβ in neurons [212–215].

3.6. Mass spectrometry imaging (MSI)

MSI is a powerful label-free technique for visualizing the spatial distribution of small metabolites, including proteins, peptides, and lipids, in tissue sections. Its superior sensitivity, high spatial resolution, and ability to provide highly informative molecular profiles make it an invaluable tool in biological research [216,217].

MSI combines two essential features: first, the specificity of mass spectrometry, which enables precise determination of molecular mass by measuring the mass-to-charge (*m/z*) ratio; and second, the capability to map the spatial distribution of these molecular species within the sample [218]. Notably, MSI has shown significant promise in studying AD pathology, offering detailed insights into the molecular changes in brain tissue, both in AD mouse models and human samples. This makes MSI a potentially invaluable technique for advancing the understanding of AD at the molecular level [219].

3.6.1. Matrix-assisted laser desorption/ionization mass spectrometry (MALDI-MS)

MALDI-MS imaging is a highly effective technique for investigating the spatial distribution of proteins and small molecules within biological tissues by enabling *in situ* analysis of tissue sections [220,221]. For example, MALDI-MS imaging can distinguish between cortical, hippocampal, and cerebellar layers while also identifying specific lipid species associated with Aβ plaques, such as sulpholipids/hexyl ceramide sulfate (SHexCer) and glycerophosphatidylinositols (GroPIn), as well as probing the spatial heterogeneity of n-streptocellulose in both mouse and human brain tissues [216,222–224]. This technique has also been used to detect Aβ species deposition in cerebral CAA and AD brains (Fig. S4c in Supporting information) [225]. Furthermore, MALDI-MS imaging has revealed the deregulation of proteostasis-related protein modules, oxidative stress, and metabolic changes in the hippocampus of early AD mice. These findings suggest that disruptions in protein modules can potentially be mitigated by early dietary intervention with ubiquinol (Fig. S4d in Supporting information) [226]. Additionally, MALDI-MS imaging has proven useful for detecting early proteomic alterations in the 5xFAD neonatal mouse model of AD, with the results showing a striking resemblance in protein expression profiles between the neonatal 5xFAD brain and AD patient specimens [220].

3.6.2. Secondary ion mass spectrometry (SIMS)

SIMS is an advanced imaging mass spectrometry technique that utilizes the kinetic energy transfer between a focused ion beam and the sample surface to generate secondary ions specific to the sample. SIMS is capable of constructing three-dimensional images of biomolecules and their associated metals without the need for external markers, making it a powerful tool for studying complex biological systems [227,228]. Specifically, time-of-flight SIMS (ToF-SIMS) is particularly adept at detecting the localization of lipids and Aβ in narrow ($\sim$10 nm) 2D planes at the tissue surface. This capability allows SIMS to extend conventional tissue imaging techniques, enabling the investigation of the intricate interplay between different molecules in AD pathology [221]. ToF-SIMS has also been employed to identify and localize cholesterol on tissue surfaces without the need for extensive pre-processing. Findings from these studies suggest that the density of NFTs is not statistically correlated with cholesterol abundance [229]. Furthermore, by using metal oxide nanoparticle-conjugated antibodies, ToF-SIMS enables the simultaneous imaging of multiple proteins associated with AD pathology [227]. Additionally, SIMS has proven effective in visualizing various lipid species, such as lyso-phosphocholine (LPC) lipids, gangliosides, and sulfatides in AD mouse models [2].

3.6.3. Others

Laser ablation-inductively coupled plasma mass spectrometry (LA-ICP-MS) has been employed for the detection and imaging of Aβ in immunohistochemical brain sections from transgenic AD mouse models, utilizing Eu- and Ni-coupled antibodies for enhanced detection [230]. Another study integrates desorption electrospray ionization (DESI) with MALDI-MS to investigate early-stage AD pathology in the brains of AD mice. The results indicate that significant alterations in lipid metabolic pathways, particularly glycerophospholipid metabolism, may play a role in the early onset of AD [231]. Gold nanoparticles anchored to porous perovskite oxide microrods (CTO@Au) have been developed as a high-performance platform for precise serum metabolic analysis, offering a robust approach for the detection of metabolic changes in AD mice [232]. In the context of AD, immunoprecipitation mass spectrometry (IP-MS) has been applied to diagnose the disease by measuring plasma Aβ42/Aβ40 ratios and Aβ amyloid levels, providing valuable diagnostic information [233,234].

Selected reaction monitoring (SRM), performed on triple-quadrupole mass spectrometers, enables the detection of low-abundance proteins in complex biological samples. Using SRM, a high-throughput method has been developed to analyze 48 key proteins in CSF [235]. Liquid chromatography-mass spectrometry (LC-MS) has been applied to accurately quantify plasma Aβ42 and Aβ40, as well as to identify the ApoE proteotype in blood samples [236]. MSI technologies have also been utilized to determine the ratio of phosphorylated tau to non-phosphorylated tau in blood, offering diagnostic accuracy comparable to clinical CSF testing for AD [237]. Using ultra-high-performance LC-MS, five metabolites, including cholic acid, chenodeoxycholic acid, allocholic acid, indolelactic acid, and tryptophan, have been identified as specific biomarkers for distinguishing AD patients from healthy controls and individuals with non-neurological disorders [238].

3.7. Spectral imaging

Spectral imaging enables the simultaneous characterization and quantification of multiple features, such as organelles and proteins, in both qualitative and quantitative terms. This technique significantly enhances the capabilities of biological and clinical research. Spectral imaging encompasses two primary components: spectroscopy and imaging. It has become a well-established tool in the diagnosis of AD, with applications in vibrational spectral imaging (VSI) and hyperspectral imaging (HSI) [239].

3.7.1. VSI

VSI is a promising label-free technique for studying protein misfolding, especially in neurodegenerative diseases like AD. Spectral imaging involves recording a spectrum at each spatial point, using dispersive optics with standard imaging systems [239–241]. Three common scanning modes are point scanning (whiskbroom), line scanning (pushbroom), and area imaging (wavelength scanning) [242]. IR spectroscopy measures molecular vibrations resulting from interactions with radiation and is applicable across varied sample states. Two main instruments used are Fourier-transform infrared (FTIR) spectrometers and dispersive spectrometers [241]. FTIR is particularly sensitive to protein secondary structure, making it ideal for detecting misfolding and aggregation [243]. In 2010, FTIR imaging visualized unsaturated lipids in the hippocampus of mouse models, revealing plaque-related pathology [69]. Micro-FTIR (μFTIR) further showed colocalization of amyloid and lipid peroxidation in AD patient tissues, emphasizing lipid oxidation's role in disease progression (Fig. S5a in Supporting information). μFTIR also detects early conformational changes in APP and Aβ [244,245]. Discrete frequency infrared imaging (DFIR) enables precise mapping of β-sheet aggregates, including those outside plaques, indicating potential diagnostic value [246].

While IR detects dipole changes, Raman detects polarizability changes, aiding protein structure analysis and amino acid residue identification in physiological settings [247–249]. Its main limitation is the inherently weak signal, but this has been mitigated

by signal-enhancing techniques such as coherent Raman scattering (CRS), surface-enhanced Raman scattering (SERS), tip-enhanced Raman scattering (TERS), and resonance Raman scattering (RRS) [250,251]. Among these, SERS is particularly powerful due to its high sensitivity, enabling simultaneous structural and concentration analysis with minimal sample preparation [252,253]. For example, silver nanogap shells (AgNGSs) serve as SERS nanoprobes for multiplex Aβ40 and Aβ42 detection in blood, outperforming ELISA in detection range [254]. A label-free ratiometric SERS platform with gold nanoparticles enables real-time imaging of Aβ aggregation by tracking I_{1244}/I_{1268} intensity ratios [255]. Similarly, SERS-LFIA biosensors quantify Aβ1–42 *via* the I_{1334}/I_{2225} ratio for accurate AD diagnosis [256]. Other probes target NO sensing using the I_{698}/I_{974} ratio in live-cell imaging [257].

CRS techniques, including coherent anti-Stokes Raman scattering (CARS) and stimulated Raman scattering (SRS), greatly amplify Raman signals. CRS allows label-free vibrational excitation, distinguishing scattered from Rayleigh light by energy shifts. In CARS, vibrational modes generate enhanced anti-Stokes signals, free from fluorescence interference and ideal for high-contrast imaging [250]. CARS imaging provides real-time, non-invasive analysis of lipids and proteins in live tissues. In AD models, it differentiates plaque regions by comparing spectral intensity ratios (Fig. S5b in Supporting information) [258,259]. SRS imaging offers label-free, high-speed chemical imaging with improved contrast over CARS due to the absence of non-resonant background signals [260–262]. In AD research, SRS detects protein misfolding by spectral shifts. For instance, blue-shifting of the amide I band by $\sim$10 cm^{-1} signifies Aβ protofibril formation. Imaging at 1640, 1658, and 1670 cm^{-1} distinguishes lipids, native proteins, and Aβ plaques (Fig. S5c in Supporting information) [240].

3.7.2. HSI

A typical HSI system consists of three main components: a light source, wavelength dispersion devices, and area detectors [262]. It has been reported that Aβ aggregates accumulate in retinal tissue during the progression of AD, and these aggregates serve as surrogate markers for brain Aβ levels [263]. HSI is well-suited to detect AD-related markers in the retina in a non-invasive, cost-effective, rapid, and label-free manner, leveraging Rayleigh light scattering (Fig. S5d in Supporting information) [264–266]. Spectral differences between healthy and transgenic AD mice, which accumulate Aβ in both the brain and retina, have been observed [265]. In another study, a reduction in short-wavelength reflectance was observed in the retinas of AD mice over time, compared to wild-type mice, due to the presence of soluble Aβ1–42 aggregates (Fig. S5e in Supporting information) [37,265–268]. In addition to Aβ plaques, phosphorylated tau has also been detected in the retinas of AD patients, further supporting the potential of HSI for label-free screening and early diagnosis of AD [267].

3.8. Multimodal imaging

Multimodal imaging integrates two or more imaging modalities within the same visualization region, offering significant advantages for both diagnostic and therapeutic applications. Ideally, distinct imaging probes can be employed to capture both structural and functional data at the same anatomical location, followed by the fusion of these images for more detailed analysis [92,173,268]. Additionally, multimodal imaging systems combine various techniques, such as MSI, MRI, vibrational spectroscopy, and fluorescence imaging, to gather extensive information on metabolic activity and molecular dynamics [269]. For example, a multimodal data fusion framework utilizing deep autoencoders and self-representation (MFASN) has been proposed for the early diagnosis of AD, through the integration of fMRI and sMRI data to construct a multimodal brain network [270]. Furthermore, combining PET with MRI allows for precise mapping of both structural and functional features in brain tissue, enhancing the diagnostic and prognostic accuracy for AD [271–273]. The integration of ^{18}F-FDG PET/CT is also valuable for studying the correlation between CSF levels of striatal dopamine transporter and regional brain metabolism, providing deeper insights into the role of dopaminergic degeneration in the pathogenesis of AD [274].

Despite the widespread use of MRI as a clinical diagnostic tool, there are currently no MRI contrast agents approved for the *in vivo* imaging of cerebral AD biomarkers [275]. Therefore, the development of multifunctional probes to enhance MRI performance for brain imaging is of significant interest. One such approach involves conjugating the well-established Aβ probe, Pittsburgh compound B (PiB), to DO3A-monoamide. This conjugation facilitates the formation of non-charged complexes with trivalent metal ions, such as Gd^{3+} for MRI applications and In^{3+} for SPECT imaging [92]. In clinical studies, three-dimensional MRI, DTI, and FDG-PET imaging have been employed to assess patients with MCI and AD. These modalities were used to evaluate hippocampal volume (HC-Vol), parahippocampal cingulum fractional anisotropy (PHC-FA), and hippocampal glucose metabolism (HC-Glu) [276]. Another study combined FDG-PET, MRI morphometry, and DTI-derived fractional anisotropy (FA) measurements in individuals with MCI [277]. Fluorescent-magnetic γ-Fe_2O_3-rhodamine or γ-Fe_2O_3-Congo red nanoparticles have emerged as promising multimodal imaging agents for Aβ detection, combining MRI and fluorescence imaging in a single nanostructured platform [91]. Additionally, theranostic Gd(DOTA)-cyanine dyad conjugates enable both one- and two-photon excited fluorescence imaging and MRI of Aβ in transgenic mouse models of AD [275]. Relying on the redox environment characteristic of AD, injections of zinc gluconate and ferrous chloride into AD mice promote the biosynthesis of fluorescent zinc oxide and magnetic iron oxide nanoclusters (Fig. 2a) [278].

The bivariate distribution of amyloid-β and tau provides insights into the underlying mechanisms of neurocognitive clinical syndromes, which can be assessed using PET-based multimodal imaging techniques. Tau aggregates predominantly accumulate in regions of the brain exhibiting hypometabolism, whereas amyloid deposits are distributed across the entire cerebral cortex [125]. Phenyl/pyridinyl-butadienyl-benzothiazole/benzothiazole (PBBs), a novel multimodal imaging agent, integrates two-photon fluorescence imaging with PET, enabling the visualization of various tau inclusions in the brains of AD patients. These findings align with the known progression of tau pathology in AD, demonstrating its widespread dissemination as the disease advances (Fig. 2b) [279].

MSI technology offers a method for monitoring spatial lipid changes *in situ*. However, the diagnosis and treatment of AD often require the integration of multifaceted pathological information to reach a definitive diagnosis. Therefore, the integration of MSI with other imaging modalities is highly advantageous for the comprehensive diagnosis of AD [280]. The high background noise and artifact signals inherent to these modalities complicate the calibration of MSI images. To address this challenge, a correlative chemical imaging strategy that combines multimodal matrix-assisted laser desorption/ionization (MALDI)-MSI, hyperspectral microscopy, and spatial chemometrics has been developed. This approach enables the high-resolution delineation of co-localized lipids and Aβ peptides within plaques, providing predictive multimodal MSI signatures that are reflective of distinct Aβ structures implicated in AD pathogenesis [269].

Dual-polarity matrix-assisted laser desorption-ionization imaging mass spectrometry (MALDI-IMS) further enhances this technique by offering high-throughput lipid molecular profiling at the same spatial resolution as individual Aβ peptide isoforms. Addi-

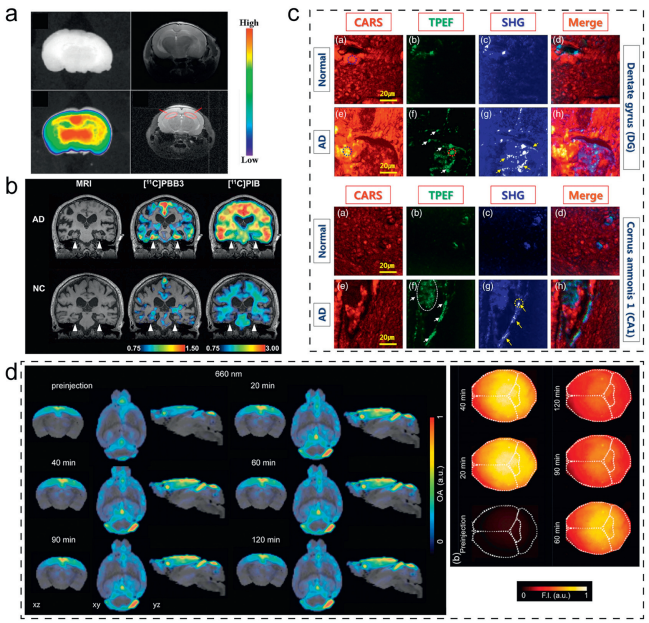


Fig. 2. Multimodal imaging for AD diagnosis. (a) Fluorescence imaging of the dissected brain from normal mice without any treatment or AD mice with the treatment of zinc gluconate and ferrous chloride solution. T2-weighted MRI imaging of the brain from normal mice with treatment of zinc gluconate or AD mice with the treatment zinc gluconate and ferrous chloride. Reproduced with permission [278]. Copyright 2017, American Chemical Society. (b) Accumulation of [^{11}C]PBB3 in the hippocampal formation of AD patients revealed by *in vitro* autoradiography and *in vivo* PET. In hippocampal formation, the [^{11}C]PBB3 retention rate is significantly increased in AD patients, in contrast to the negligible change in NC patients. Reproduced with permission [279]. Copyright 2013, Elsevier Inc. (c) Comparison of typical multimodal multiphoton microendoscope images of normal and AD samples from hippocampal dentate gyrus region. Reproduced with permission [284]. Copyright 2015, SPIE. (d) *In vivo* hybrid 3D vMSOT and epifluorescence imaging of CRANAD-2 in an Aβ mouse. Reproduced with permission [147]. Copyright 2021, Elsevier B.V.

tionally, structural diversity among Aβ plaques can be detected, along with other chemical species, including neuronal lipids, using both MALDI-IMS and fluorescence imaging [217]. These findings manifest the significant role of lipid disturbances, including sphingolipid metabolism, in the pathophysiology of AD [281]. To further investigate the molecular basis of Aβ aggregation in AD, an integrated tetramodal chemical imaging approach has been developed, which incorporates trimodal MSI along with interlaced fluorescence microscopy from a single tissue section. Characteristic patterns of plaque-associated lipid and peptide localizations in AD models can be elucidated by analyzing multimodal imaging and multivariate data [282].

An acoustic wave-based acoustofluidic separation device has been developed to isolate and purify AD biomarkers, enhancing the signal-to-noise ratio through SERS and electrochemical immunosensing. The diagnostic accuracy and reliability of these multimodal biosensors are significantly improved, positioning them as potentially viable clinical translational devices for early AD diagnosis [283]. Furthermore, multicolor imaging of AD brain samples has been achieved by integrating two-photon excited fluorescence and second-harmonic generation on a CARS microendoscope platform. Analysis of two hippocampal regions, the cornu ammonis-1 (CA1) and dentate gyrus, revealed that lipids, amyloid fibrils, and collagen are more abundant in AD samples compared to NCs (Fig. 2c) [284].

Label-free optical techniques offer a direct means of detecting elemental and biochemical changes with high reliability and precision, owing to their high resolution, intrinsic contrast, and minimal sample preparation. Multimodal biospectroscopic approaches, such as XFM and FTIR spectroscopy, enable the identification of significant biochemical and elemental alterations and their colocalizations within specific cerebral regions [213]. Notably, the combination of FTIR, Raman microscopy, and XFM has provided substantial complementary information on the biochemical and elemental composition of Aβ plaques. This multimodal imaging approach does not require complex tissue fixation or staining, allowing for the comprehensive analysis of key components, including aggregated proteins, lipids, cholesterol, and metal ions [285].

The integration of fluorescence spectroscopy, atomic force microscopy (AFM) imaging, and circular dichroism (CD) spectroscopy provides a powerful approach to investigating the selective binding of molecularly imprinted nanoparticle (MINP) receptors to specific segments of Aβ40 [286]. Additionally, the curcumin derivative CRANAD-2 is employed for detecting Aβ deposition in transgenic AD mouse models using multi-spectral optoacoustic tomography and fluorescence imaging. CRANAD-2 demonstrates specific and quantitative detection of Aβ fibrils *in vitro*, with the ability to differentiate between monomeric and fibrillar forms of Aβ (Fig. 2d) [147]. Furthermore, nanogel probes, such as SPIO@GCS/acryl/biotin-CAT/SOD-gel (SGC) and BRET-FRET nanobubbles, are utilized for imaging inflammation through US imaging/MRI and US imaging/bioluminescence, respectively [150,287].

Spectral imaging is a crucial component of multimodal imaging, with the combination of spectral and fluorescence imaging being the most widely studied. The integration of two-photon excitation fluorescence (TPEF) microscopy and CARS enables long-term imaging of Aβ plaques and blood vessels in AD mouse models, facilitating the study of both physiological and disease conditions to extract essential structural and functional information [288]. The biochemistry of Aβ plaques, including their chemical signatures and the presence of oxidized lipids, can be characterized through the combined application of FTIR spectroscopy, Raman spectroscopy, and immunofluorescence imaging [246]. The elemental distribution and fibrillar structure of Aβ plaques in neurons can be assessed by combining optical photothermal infrared (O-PTIR) and synchrotron-based X-ray fluorescence (S-XRF) nano-imaging techniques [212]. Additionally, the use of hyperspectral snapshot cameras and optical coherence tomography (OCT) allows for the accurate determination of retinal nerve fiber layer (RNFL) thickness. The relationship between retinal structure and cognitive function can be clarified through standardized and longitudinal data analysis from amyloid-phenotyped cohorts [289].

3.9. Nanoparticle-based imaging strategies

Recent advances in nanotechnology have significantly improved the early diagnosis of AD, particularly through the development of nanoparticle-based imaging strategies. These approaches leverage the unique physical and chemical properties of engineered nanomaterials to enable non-invasive, highly sensitive, and target-specific imaging of pathological biomarkers such as Aβ plaques and tau protein aggregates. Based on material composition and function, these strategies can be categorized into several main classes: magnetic nanoparticles, gold nanoparticles, QDs and fluorescent nanoprobes, polymeric/liposomal nanoparticles, and hybrid theranostic nanostructures.

Magnetic nanoparticles (MNPs) have gained prominence as contrast agents for MRI due to their strong magnetic susceptibility and ability to enhance signal contrast. MNPs can be functionalized with specific ligands or peptides that facilitate BBB penetration and targeting of AD-related biomarkers, such as Aβ plaques and regions of neuroinflammation. Chaparro *et al.* highlighted the theranostic potential of MNPs, demonstrating their dual utility in imaging and treatment [290]. Similarly, Jiang *et al.* developed neuroinflammation-targeted MNPs that successfully enabled early-

stage detection of AD through enhanced MRI sensitivity and specificity [291]. AuNPs, particularly in rod or spherical forms, have been extensively utilized for optical and CT imaging due to their unique surface plasmon resonance (SPR) properties. Morales-Zavala *et al.* demonstrated the application of GNRs in micro-CT imaging *in vivo*, showing not only the effective visualization of amyloid burden but also a therapeutic decrease in plaque load, emphasizing their value as a neurotheranostic platform for AD [292].

QDs and fluorescent nanoprobes offer significant advantages in optical imaging due to their bright fluorescence, tunable emission spectra, and stability. These properties allow for the ultra-sensitive detection of AD biomarkers at very low concentrations. Agraharam *et al.* discussed the use of QDs in FRET and SERS imaging to detect both Aβ and tau proteins in early disease stages [293]. The ability of QDs to be conjugated with biomolecular probes provides a flexible platform for highly specific, multiplexed imaging. Polymeric nanoparticles and liposomes represent another important class of nanocarriers for imaging agents. Song *et al.* reviewed the potential of polymeric systems to encapsulate both therapeutic and diagnostic agents, achieving targeted imaging of AD-related biomarkers [294].

Hybrid or multi-material nanostructures, often described as theranostic platforms, are engineered to simultaneously perform diagnostic imaging and deliver therapeutic agents. These multifunctional nanoparticles often integrate inorganic cores (such as magnetic or gold components) with polymeric or lipid-based shells, offering synergistic capabilities in targeting, imaging, and therapy. Panghal and Flora emphasized the significance of such systems in enabling simultaneous visualization and treatment of AD pathology [295]. Dai *et al.* and Li *et al.* further discussed recent developments and the bibliometric landscape of nanotheranostics in AD, highlighting the rapid growth of hybrid nanoparticle research and the push toward multifunctional platforms that bridge diagnostics and treatment [296,297].

3.10. Summary of imaging modalities

Further investigation into AD pathogenesis and the refinement of molecular mechanisms are essential to drive the development of more advanced therapeutic approaches for AD [7]. Although CSF analysis demonstrates high accuracy in the early diagnosis of AD, the invasive nature of lumbar puncture for CSF collection, which often causes discomfort and reduces patient compliance. Emerging evidence indicates that blood biomarkers, such as P-tau, Aβ1–40, and Aβ1–42, are correlated with AD pathology in brain tissue. However, detecting AD biomarkers at low concentrations in blood remains challenging due to limited sensitivity and interference from the blood matrix composition, which impairs detection performance [5]. To address these issues, non-invasive imaging techniques are being developed to provide solutions. Although PET has become the primary *in vivo* technique for amyloid detection and early AD diagnosis, its spatial resolution is relatively low, and image quality is often compromised by substantial noise. Fluorescence and PA imaging are emerging as cost-effective and safe alternatives, as they do not require extensive infrastructure. However, the number of endogenous fluorophores present in human tissue is extremely limited, and the targeted delivery of exogenous fluorophores presents significant challenges, which compromises both sensitivity and specificity [36,147]. In contrast, vibrational spectroscopy detects molecular vibrational frequencies without the need for dyes or extrinsic labeling. While infrared microscopy has the potential to detect protein aggregation and lipid homeostasis, its application is constrained by low sensitivity, limited spatial resolution, and infrared absorbance [298]. FTIR spectroscopy is capable of detecting protein aggregation and lipid disturbances, while Raman spectroscopy offers higher spatial resolution for imaging lipids, particularly cholesterol, but suffers from prolonged acquisition times despite efforts to accelerate signal capture [299]. XFM is capable of detecting a broad range of transition metals such as iron, copper, and zinc [288]. HSI can identify Aβ-containing aggregates in retinal tissue [263]. To overcome the limitations of individual imaging modalities, multimodal imaging, which combines two or more imaging techniques, has emerged as a powerful strategy for obtaining comprehensive information on AD pathology (Table 1).

4. Imaging-guided AD therapy

For decades, therapeutic strategies have primarily targeted the pathological features of AD, with a focus on the targeted delivery of monoclonal antibodies to Aβ plaques or oligomers [31]. The integration of imaging modalities in the therapeutic process can contribute to achieving more precise treatment outcomes, surpassing conventional therapies by enhancing biosafety and improving efficacy [300]. Imaging-guided therapy could enhance the uniformity of drug dosing and optimize drug utilization, enabling the assessment of both dosimetric and non-dosimetric factors at the lesion site. The use of molecular probes during treatment allows for the evaluation of drug biodistribution, delivery efficiency, as well as clearance and excretion profiles, offering a comprehensive approach to therapeutic management [301]. The PET modality serves as a critical link between the molecular mechanisms underlying AD pathology and targeted therapeutic interventions. Taking the advantages of precise targeting, accurate dose delivery, minimal toxicity, and enhanced therapeutic efficacy, PET image-guided drug delivery has been widely employed in the treatment of conditions such as rheumatoid arthritis, cancer, and infections [302].

The BBB prevents the majority of pharmaceuticals from crossing into the extracellular fluid of the CNS [303,304]. MRI-guided focused US (MRIgFUS) has emerged as a pivotal non-invasive technique for transiently opening the BBB in targeted regions, thereby facilitating the efficient delivery of therapeutic agents to the brain [153,305,306]. For instance, MRIgFUS-mediated enhancement of BBB permeability enables the delivery of the neuroprotective agent D3, which counteracts neurodegeneration in AD through activation of the TRKA-related signaling cascade (Fig. 3a) [307]. Subsequent prognostic evaluations show that the BBB in AD patients returns to a normal state without causing further impairment [148–151]. MRIgFUS also facilitates passive immunization with a novel 2 N tau isoform-specific single-chain antibody fragment, RN2N, which reduces anxiety-like behavior and the phosphorylation of tau at specific sites [308]. When combined with microbubbles, MRIgFUS offers a targeted and non-invasive approach to BBB disruption. For example, the combination of low-intensity focused US and microbubble contrast agents, guided by real-time MRI imaging, transiently opens the BBB, enabling the precise delivery of fluorophores and immunotherapeutics to amyloid plaques with minimal tissue damage [309]. The surface properties of Fe-MIL-88B-NH2-NOTA-DMK6240/MB enhance MRI capability and improve AD symptoms by preventing hyperphosphorylated tau aggregation and neuronal death (Fig. 3b) [310]. Transcranial pulse stimulation (TPS), a novel technique involving single ultrashort US pulses at frequencies of 200–300 ms, differs from focused US and has been shown to significantly improve neuropsychological scores in AD patients, with curative effects maintained for up to three months based on functional MRI data [311].

Fluorescence image-guided therapy for AD has been extensively explored with a view toward clinical application. For example, RVG-modified neural stem cell membrane-coated nanoparticles (NSCs) encapsulated with AgAuSe QDs have been developed for the pharmacological treatment of AD, with real-time monitoring *via* multiscale NIR-II imaging (Fig. 3c) [187]. Additionally,

Table 1
Comparison of imaging modalities for AD diagnosis.

Imaging modality	Imaging principle	Spatial resolution	Specificity to Aβ/Tau	Stage of application	Remarks
MRI	Proton relaxation in magnetic field	High (0.1–1 mm)	Low (without contrast agent)	Structural and vascular changes	Excellent anatomical context, limited molecular specificity
PET	Detection of radiolabeled probe decay (γ-rays)	Moderate (4–6 mm)	High	Clinical diagnosis and staging	Highly sensitive, Aβ and tau tracers available
SPECT	Detection of γ-rays from radiotracers	Lower than PET (8–10 mm)	Moderate	Functional imaging	Longer half-life isotopes, lower cost than PET
US	Reflection of high-frequency sound waves	Moderate (0.1–1 mm)	Low (improved with contrast)	Emerging/preclinical	Non-invasive and portable, BBB modulation possible
PA	Optical absorption converted to acoustic signal	High (50–200 μm)	Moderate (depends on agent)	Preclinical/early-stage	Good depth and resolution, requires exogenous agents
Fluorescence Imaging	Emission of light from fluorescent probes	High (10–100 μm)	High (probe-dependent)	Preclinical and intraoperative	Limited by penetration and photobleaching
MSI	Mass-to-charge analysis of molecular species	Very high (cellular level)	Very high	Postmortem analysis	Multiplexed, spatially resolved molecular profiling
Multimodal Imaging	Integration of two or more modalities (*e.g.*, PET/MRI)	Varies (modality-dependent)	High	Advanced preclinical/clinical	Combines anatomical, functional, and molecular information

aggregation-induced emission (AIE) nanotherapeutic agents have been designed for targeted AD treatment [312]. The binding of these nanotheranostics to amyloid plaques inhibits Aβ fibril formation, degrades existing fibrils, and prevents reaggregation. Self-fluorescent monochrome nanoparticles (TNPs), composed of amino acids, can label and detect diphenylalanine and Aβ42 peptide fibrils due to their intrinsic fluorescence properties. Moreover, TNPs have shown the potential to inhibit peptide aggregation and alleviate Aβ-induced cytotoxicity [313]. Furthermore, ultrathin zinc selenide (ZnSe) nanoplatelets have been engineered to monitor brain copper levels in AD mice using PA imaging, while simultaneously reducing oxidative stress in neurons to restore neurological function (Fig. 3d) [161]. To enhance the properties of nanoagents lacking inherent fluorescence, a nanosystem (FGL-NP(Cit)/HNSS) modified with an FGFR1 ligand, FGL peptide, has been developed for enhanced brain accumulation (4.8-fold) and preferential distribution to cholinergic neurons in AD-affected regions. This system is responsive to mild acidity, triggering lysosomal escape and controlled intracellular drug release in neurons [314]. Thioflavin T (ThT), a β-amyloid-specific dye, modified graphene oxide and iron oxide nanoparticles (GOIO) have been shown to reduce Aβ aggregation and mitigate the toxicity of Aβ fibrils to neuroblastoma cells, with the process being monitored *via* fluorescence imaging [315]. Additionally, PEGylated silica nanoparticles (PSiNPs) have demonstrated the ability to cross the BBB for non-invasive *in vivo* or *ex vivo* fluorescence imaging, facilitating drug delivery and enhancing therapeutic outcomes [316].

Image-guided photothermal therapy (PTT) is an effective therapeutic strategy with high diagnostic accuracy, enabling the monitoring of photothermal agent accumulation at lesion sites and determination of the optimal treatment window. A novel macromolecular fluorophore, formed by conjugating a small-molecule NIR-II fluorophore (Flav7) with an amphiphilic polypeptide, has shown promise for the visualization of Aβ fibrils using NIR-II fluorescence, while also producing significant photothermal ablation effects for AD treatment (Fig. 3e) [317]. Additionally, photothermal reagents such as PDA-Ru, KLVFF@Au-CeO_2, and Ru@Pen@PEG-AuNS have been utilized for NIR/PA imaging, with demonstrated ability to decompose Aβ fibers [318–320]. GO-ThS nanomaterials have been shown to induce dissociation of aggregated amyloid plaques through hyperthermia upon NIR light irradiation, with real-time monitoring of the morphological changes of Aβ fibrils [321]. Chlorin e6 (Ce6) and immunoglobulin G (IgG) can self-assemble into nanocomplexes that enable fluorescence image-guided photodynamic therapy (PDT) and immunotherapy for AD [322,323]. Metal-organic framework-derived carbon (MOFC) materials, exhibiting NIR light-responsive PA properties, have demonstrated the ability to transform robust, β-sheet-dominant neurotoxic Aβ aggregates into non-toxic debris, providing a promising approach for AD treatment [322].

Magnetic thermotherapy, when combined with magnetic particle imaging (MPI), offers an image-guided therapeutic platform that allows for precise targeting of pathological cells while minimizing non-specific damage to healthy tissues. Magnetic nanoparticles, delivered specifically to the lesion site, can be activated by an alternating magnetic field (AMF), resulting in localized heat generation for magnetothermal treatment. For example, SPIONs used as tracers in MPI can be excited to produce heat for magnetic hyperthermia, facilitating the accurate localization and treatment of diseases (Fig. 3f) [323]. The integration of multiple imaging modalities addresses the inherent limitations of each individual modality, thereby enhancing both diagnostic and therapeutic capabilities for various diseases [300,324,325]. A theranostic Gd(DOTA)-cyanine dyad is used for imaging Aβ plaques in AD mouse models. This probe not only enables imaging but also demonstrates the ability to inhibit Aβ aggregation and reduce Aβ-induced ROS gen-

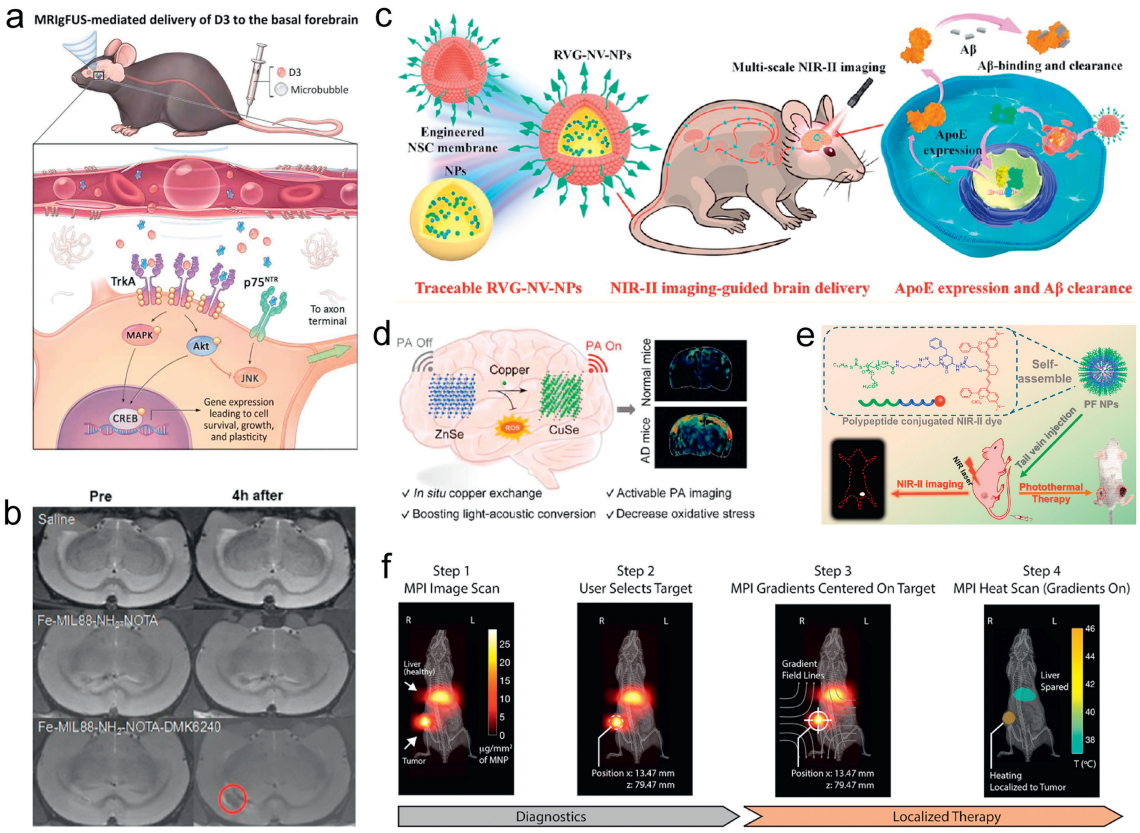


Fig. 3. Imaging-guided AD therapy. (a) Scheme to illustrate the MRIgFUS delivery of D3, a selective TrkA agonist, to the basal forebrain to rescue neurotrophin signaling and cholinergic function in AD mice. Reproduced with permission [307]. Copyright 2020, AAAS. (b) T2-weighted MRI images of AD mice after administration of Fe-MIL-88B-NH2-NOTA, Fe-MIL-88B-NH2-NOTA-DMK6240, and saline for 4 h. Reproduced with permission [310]. Copyright 2020, American Chemical Society. (c) Scheme of genetically engineered NSCs membrane-camouflaged nanocomplex (RVG-NV-NPs) and its applications in CNS drug delivery. Reproduced with permission [187]. Copyright 2023, American Chemical Society. (d) Scheme to illustrate the concept of ultrathin zinc selenide (ZnSe) nano-ions for monitoring brain copper levels and treatment AD. Reproduced with permission [161]. Copyright 2022, American Chemical Society. (e) Schematic diagram of the mechanism of NIR image-guided photothermal therapy. Schematic illustration of the mechanism of the NIR image-guided PTT by a facile macromolecular fluorophore. Reproduced with permission [317]. Copyright 2019, American Chemical Society. (f) *In vivo* experimental demonstration of localization of magnetic hyperthermia using SPIONs. Reproduced with permission [323]. Copyright 2018, American Chemical Society.

eration [275]. Furthermore, the curcumin-derivative CRANAD-2 has been developed for multispectral optoacoustic tomography and fluorescence imaging of brain Aβ deposits in AD cerebral amyloidosis models, such as arcAβ mouse models [147].

5. Current limitations and future perspectives

In the current landscape of imaging technologies for AD, each modality offers unique strengths and limitations in terms of sensitivity, specificity, and clinical applicability. Optical imaging, while highly sensitive, is limited to preclinical use due to poor tissue penetration. US imaging is hindered by skull interference and remains unsuitable for brain diagnostics. PET and SPECT provide high sensitivity and target specificity but are limited by radiation exposure, high cost, and limited accessibility, making them less ideal for routine screening. In contrast, MRI and CT show strong potential for broader clinical use. MRI offers excellent spatial resolution and anatomical detail, and its molecular imaging capabilities are expanding through the development of targeted contrast agents such as gadolinium-based probes and SPIONs. CT, particularly with dual-energy or spectral techniques, has been explored for amyloid imaging using high-atomic-number contrast agents. Despite promising advances, MRI and CT imaging probes still face challenges related to sensitivity, target specificity, and BBB penetration. Ongoing research into optimized probe design and clinically translatable agents will be critical for realizing the full diagnostic potential of these platforms in AD.

PA imaging bridges optical contrast with acoustic resolution, enabling high-resolution imaging of vascular and molecular changes with moderate depth penetration. It shows growing promise in detecting Aβ-related pathology but remains limited in deep brain applications. Fluorescence imaging allows real-time visualization with high sensitivity; yet, its application is challenged by limited tissue penetration, potential photobleaching, and autofluorescence interference. MSI provides unparalleled molecular specificity and multiplexed biomarker profiling, including spatial distributions of Aβ and tau species, but it is inherently a post-mortem, label-free modality unsuitable for *in vivo* monitoring. Multimodal imaging strategies have emerged as promising solutions, combining complementary strengths of two or more techniques, to enhance diagnostic accuracy, anatomical context, and molecular characterization. Nonetheless, these platforms are still evolving, with challenges in integration, probe compatibility, and clinical scalability.

One of the most formidable challenges in the development of imaging agents for AD lies in the effective traversal of the BBB, a selective physiological barrier that limits the entry of diagnostic and therapeutic agents into the brain parenchyma. Recent advancements in nanotechnology have introduced a range of innovative strategies to overcome this limitation. Various nanomaterials, such as liposomes, polymeric nanoparticles, and metal-based systems, have been engineered with physicochemical properties tailored to enhance BBB permeability, often through mechanisms such as receptor-mediated transcytosis or surface functionalization

with targeting ligands [326–328]. These nanoplatforms not only improve the transport of imaging probes across the BBB but also stabilize the probes in circulation, reducing off-target effects and enhancing signal specificity.

Multifunctional nanocarriers that integrate diagnostic and therapeutic modalities have demonstrated particular promise. For example, nanostructures with high surface area and modifiable surfaces have been shown to increase both brain uptake and contrast efficiency in imaging Aβ and tau pathologies [327,329]. Moreover, MNPs and QDs exhibit intrinsic imaging properties that, when functionalized appropriately, can target specific AD biomarkers while navigating the restrictive BBB environment [329]. Lipid-based nanoparticles and dendrimers also offer favorable biodistribution and BBB penetration profiles, making them suitable vehicles for imaging agents as well as therapeutic payloads [330]. Importantly, ongoing research has explored surface modifications that enhance nanoparticle interaction with endothelial receptors, enabling more efficient brain delivery even under pathological conditions where BBB integrity is variably altered [327,331]. Despite these advancements, several limitations remain. Many nanomaterials still face challenges related to biocompatibility, long-term safety, and scale-up production for clinical translation. Furthermore, while animal models show promising results, the human BBB presents additional complexities that may reduce translational efficacy. Therefore, future work should focus on refining nanoparticle design for increased targeting precision, minimizing potential toxicity, and validating performance through well-controlled clinical studies [326–331].

Looking forward, one of the most promising directions in the imaging-based diagnosis of AD lies in the advancement of personalized diagnostic strategies. As our understanding of AD heterogeneity deepens in recognizing the differences in biomarker expression, disease progression rates, and comorbidities. There is growing recognition that a one-size-fits-all imaging approach is insufficient. Future developments are expected to take account of patient-specific molecular profiles, integrating multimodal imaging data (*e.g.*, Aβ, tau, neuroinflammation, and metabolic signatures) with genetic risk factors and clinical phenotypes to tailor diagnostic protocols. Artificial intelligence and machine learning algorithms are increasingly being deployed to analyze complex, longitudinal datasets and predict disease trajectories on an individual level. Furthermore, personalized imaging probes that target unique biomarker combinations or respond to microenvironmental cues (such as pH or oxidative stress) hold promise for improving early detection and monitoring therapeutic response. As precision medicine principles are progressively integrated into neurodegenerative disease management, the future of AD imaging will likely shift from population-based diagnostics toward patient-tailored, adaptive imaging frameworks that enhance both accuracy and clinical relevance.

Recent progress in artificial intelligence (AI)-assisted neuroimaging has opened promising avenues for enhancing early diagnosis and precision in AD. Deep learning and explainable AI models have demonstrated significant potential in detecting subtle neurodegenerative patterns, particularly in early-stage AD, by extracting high-dimensional features from structural MRI, PET, and retinal imaging data that are often imperceptible to the human eye [332–338]. These technologies facilitate not only more accurate classification of AD subtypes but also interpretation transparency, as seen in the integration of explainable frameworks to improve clinical trust and adoption [332,337]. Moreover, the fusion of multimodal data, including structural imaging, histopathology, and even retinal biomarkers, has emerged as a powerful strategy to overcome the limitations of single-modality approaches [334,335,338]. Future directions point toward the convergence of digital pathology and radiological imaging, enabling integrated diagnostic systems that link image-based phenotypes with tissue-level pathology, supported by AI-driven algorithms capable of learning from cross-domain datasets [337]. This cross-disciplinary synergy is anticipated to not only accelerate early lesion detection and individualized risk prediction but also to reshape the diagnostic landscape toward a more multi-scale, data-integrated model of AD diagnosis and progression monitoring [333,335,338].

Imaging-guided therapy represents a rapidly evolving frontier in AD research, offering the potential to precisely monitor therapeutic response and optimize intervention timing. Advanced neuroimaging modalities such as PET and MRI are increasingly being used not only for diagnosis but also to assess dynamic changes in Aβ and tau deposition following treatment, allowing real-time feedback on drug efficacy. Molecular imaging agents targeting neuroinflammation, synaptic activity, and metabolic dysfunction further expand the ability to personalize therapeutic strategies and track off-target effects. By combining diagnostic imaging and targeted drug delivery, theranostic nanoplatforms are being developed to enable spatially and temporally controlled treatment of AD pathology. These approaches facilitate the visualization of drug distribution and accumulation within specific brain regions, ensuring precise targeting of affected areas while minimizing systemic exposure. As the field advances, integrating imaging biomarkers into therapeutic decision-making frameworks will be essential for moving toward adaptive, individualized treatment paradigms that respond dynamically to disease progression and treatment response.

6. Conclusion

AD is the result of a complex interplay of multiple interrelated pathological factors, severely impacting the health of individuals over the age of 65 and posing a significant global health challenge. While the precise contributions of key pathological features, such as Aβ plaques and NFTs, to brain damage in AD remain a topic of ongoing debate, research into the determinants of AD progression and effective therapies is actively ongoing. The continuous development and refinement of various imaging technologies have greatly enhanced their utility in investigating neurodegenerative diseases, providing invaluable tools to explore the underlying pathology of AD in greater detail. This review summarizes the diverse imaging modalities used for AD diagnosis, highlighting their respective advantages and limitations. Moreover, the integration of multiple imaging techniques holds considerable promise for advancing the understanding of AD pathogenesis and progression by enabling the concurrent detection of disruptions in cellular metabolism, signaling pathways, and structural integrity. The review also briefly discusses the emerging field of image-guided therapy for AD. In contrast to diagnostic imaging, research on image-guided therapeutic strategies remains in its early stages, with significant gaps remaining in areas such as MSI, spectral imaging, and other advanced techniques. These areas warrant further investigation to optimize their application in clinical settings. Ultimately, there is a pressing need to develop more refined imaging-guided therapeutic approaches to enhance AD management. Such approaches could not only improve patient outcomes but also reduce treatment durations, providing a more effective means of combating this devastating disease.

Declaration of competing interest

The authors declare that they have no known competing financial interests or personal relationships that could have appeared to influence the work reported in this paper.

CRediT authorship contribution statement

Xingli Zhang: Writing – original draft, Methodology, Investigation, Data curation. **Peng Xue:** Writing – review & editing, Supervision, Project administration, Funding acquisition, Conceptualization.

Acknowledgments

This study is supported by Key Research and Development Project of Sichuan Provincial Science and Technology Plan (No. 2024YFFK0249), Open Research Project from Anhui Provincial Key Laboratory of Tumor Evolution and Intelligent Diagnosis and Treatment (No. KFKT202405), and Scientific and Technological Research Program of Chongqing Municipal Education Commission (No. KJQN202400202).

Supplementary materials

Supplementary material associated with this article can be found, in the online version, at doi:10.1016/j.cclet.2025.111628.

References

[1] H.T. Beier, C.B. Cowan, I.H. Chou, et al., Plasmonics 2 (2007) 55–64.
[2] T. Demeritte, B.P. Viraka Nellore, R. Kanchanapally, et al., ACS Appl. Mater. Interfaces 7 (2015) 13693–13700.
[3] M. Hadjidemetriou, J. Rivers-Auty, L. Papafilippou, et al., ACS Nano 15 (2021) 7357–7369.
[4] G. Eskici, P.H. Axelsen, Biochemistry 51 (2012) 6289–6311.
[5] S.J. Yang, J.U. Lee, M.J. Jeon, S.J. Sim, Anal. Chim. Acta 1195 (2022) 339445.
[6] I.H. Chou, M. Benford, H.T. Beier, et al., Nano Lett. 8 (2008) 1729–1735.
[7] K.H.P. Vu, M.C. Lee, G.H. Blankenburg, et al., Anal. Chem. 93 (2021) 16320–16329.
[8] H. Gao, J. Wang, J. Liu, et al., ACS Chem. Neurosci. 12 (2021) 4257–4264.
[9] Y. Zhou, Z. Song, X. Han, H. Li, X. Tang, ACS Chem. Neurosci. 12 (2021) 4209.
[10] S. Teipel, A. Drzezga, M.J. Grothe, et al., Lancet Neurol. 14 (2015) 1037–1053.
[11] A. Zengin, U. Tamer, T. Caykara, Biomacromolecules 14 (2013) 3001–3009.
[12] S.X. Zhou, H. Zhou, P.J. Walian, B.K. Jap, Biochemistry 46 (2007) 2553–2563.
[13] M.M. Gessel, S. Bernstein, M. Kemper, D.B. Teplow, M.T. Bowers, ACS Chem. Neurosci. 3 (2012) 909–918.
[14] N. Puentes-Díaz, D. Chaparro, D. Morales-Morales, A. Flores-Gaspar, J. Alí-Torres, ACS Omega 8 (2023) 4508–4526.
[15] P. Paudel, S.H. Seong, Y. Zhou, et al., ACS Omega 4 (2019) 12259–12270.
[16] J. Kiskis, H. Fink, L. Nyberg, et al., Sci. Rep. 5 (2015) 13489.
[17] H. Rai, S. Gupta, S. Kumar, et al., J. Med. Chem. 65 (2022) 8550–8595.
[18] F. Gao, Eur. J. Radiol. 145 (2021) 110017.
[19] E.C.B. Johnson, E.B. Dammer, D.M. Duong, et al., Nat. Med. 26 (2020) 769–780.
[20] G. Biechele, B.S. Rauchmann, D. Janowitz, et al., J. Neuroinflamm. 21 (2024) 30.
[21] G.D. Stanciu, A. Luca, R.N. Rusu, et al., Biomolecules 10 (2019) 40.
[22] M. Padurariu, A. Ciobica, R. Lefter, et al., Psychiatr. Danub. 25 (2013) 401–409.
[23] L. Tillement, L. Lecanu, V. Papadopoulos, Mitochondrion 11 (2011) 13–21.
[24] Y. Liu, M. Nguyen, A. Robert, B. Meunier, Acc. Chem. Res. 52 (2019) 2026–2035.
[25] A.T. Kodamullil, F. Zekri, M. Sood, et al., Nat. Rev. Drug Discov. 16 (2017) 819.
[26] Z. Liu, Q. Liu, B. Zhang, et al., J. Med. Chem. 64 (2021) 13853–13872.
[27] P. Dao, F. Ye, Y. Liu, et al., ACS Chem. Neurosci. 8 (2017) 798–806.
[28] A. Robert, Y. Liu, M. Nguyen, B. Meunier, Acc. Chem. Res. 48 (2015) 1332–1339.
[29] J. Cai, P. Yi, Y. Miao, et al., ACS Appl. Mater. Interfaces 12 (2020) 26812–26821.
[30] Y. Li, E. Lim, T. Fields, et al., ACS Biomater. Sci. Eng. 5 (2019) 3595–3605.
[31] A. Nandakumar, Y. Xing, R.R. Aranha, et al., Biomacromolecules 21 (2020) 988–998.
[32] F. Bisceglia, F. Seghetti, M. Serra, et al., ACS Chem. Neurosci. 10 (2018) 1420–1433.
[33] Y. Yang, D. Arseni, W. Zhang, et al., Science 375 (2022) 167–172.
[34] Y.W. Jun, S.W. Cho, J. Jung, et al., ACS Cent. Sci. 5 (2019) 209–217.
[35] M.G. Savelieff, S. Lee, Y. Liu, M.H. Lim, ACS Chem. Biol. 8 (2013) 856–865.
[36] F. Peccati, S. Pantaleone, V. Riffet, et al., J. Phys. Chem. B 121 (2017) 8926–8934.
[37] S.S. More, R. Vince, ACS Chem. Neurosci. 6 (2014) 306–315.
[38] W. Zhen, H. Han, M. Anguiano, et al., J. Med. Chem. 42 (1999) 2805–2815.
[39] C. Duyckaerts, B. Delatour, M.C. Potier, Acta Neuropathol. 118 (2009) 5–36.
[40] E.K. Agyare, S.R. Leonard, G.L. Curran, et al., Mol. Pharm. 10 (2013) 1557–1565.
[41] S.S. More, A.P. Vartak, R. Vince, ACS Chem. Neurosci. 4 (2012) 330–338.
[42] H. Chen, S. Liu, S. Li, et al., ACS Chem. Neurosci. 9 (2018) 1560–1565.
[43] L. Zhu, L. Xu, X. Wu, et al., ACS Appl. Mater. Interfaces 13 (2021) 23328–23338.
[44] Y. Miller, B. Ma, R. Nussinov, Biochemistry 50 (2011) 5172–5181.
[45] D. Chu, F. Liu, ACS Chem. Neurosci. 10 (2018) 931–944.
[46] M. Sadqi, F. Hernández, U. Pan, et al., Biochemistry 41 (2002) 7150–7155.
[47] B. Pan, X. Lu, X. Han, et al., ACS Omega 6 (2021) 31782–31796.
[48] H.Y. Qureshi, T. Li, R. MacDonald, et al., Biochemistry 52 (2013) 6445–6455.
[49] M.D.C. Cárdenas-Aguayo, L. Gómez-Virgilio, S. DeRosa, M.A. Meraz-Ríos, ACS Chem. Neurosci. 5 (2014) 1178–1191.
[50] S. Ahmadi, S. Zhu, R. Sharma, et al., ACS Omega 4 (2019) 5356–5366.
[51] A. Soragni, B. Zambelli, M.D. Mukrasch, et al., Biochemistry 47 (2008) 10841–10851.
[52] D. Yugay, D.P. Goronzy, L.M. Kawakami, et al., Nano Lett. 16 (2016) 6282–6289.
[53] C. Ghosh, M. Seal, S. Mukherjee, S.G. Dey, Acc. Chem. Res. 48 (2015) 2556–2564.
[54] C. Ghosh, D. Pramanik, S. Mukherjee, A. Dey, S.G. Dey, Inorg. Chem. 52 (2012) 362–368.
[55] L. Lai, C. Zhao, M. Su, et al., Biomater. Sci. 4 (2016) 1085–1091.
[56] E. Akyuz, A. Arulsamy, F.S. Aslan, et al., Mol. Neurobiol. 62 (2025) 1631–1674.
[57] S. He, X. Zhang, S. Qu, ACS Chem. Neurosci. 10 (2018) 175–181.
[58] A. Sánchez-Melgar, J.L. Albasanz, M. Pallàs, M. Martín, ACS Chem. Neurosci. 11 (2020) 1770–1780.
[59] J.L. Albasanz, E. Dalfó, I. Ferrer, M. Martín, Neurobiol. Dis. 20 (2005) 685–693.
[60] M. Renner, P.N. Lacor, P.T. Velasco, et al., Neuron 66 (2010) 739–754.
[61] R. Jarosova, S.S. Niyangoda, P. Hettiarachchi, M.A. Johnson, ACS Chem. Neurosci. 13 (2022) 2924–2931.
[62] Y. Yang, L. Zhang, J. Wang, et al., Anal. Chem. 94 (2022) 13498–13506.
[63] J. del Pino, J. Marco-Contelles, F. López-Muñoz, A. Romero, E. Ramos, ACS Chem. Neurosci. 9 (2018) 2880–2885.
[64] J. Frandsen, S.R. Choi, P. Narayanasamy, ACS Chem. Neurosci. 11 (2020) 356–366.
[65] S. Mondal, Y. Vashi, P. Ghosh, et al., ACS Chem. Neurosci. 11 (2020) 3277–3287.
[66] H.J. Kwon, M.Y. Cha, D. Kim, et al., ACS Nano 10 (2016) 2860–2870.
[67] M.P. Singulani, C.P.M. Pereira, A.F.F. Ferreira, et al., Exp. Gerontol. 133 (2020) 110882.
[68] R. Tao, M. Liao, Y. Wang, et al., Anal. Chem. 94 (2021) 1308–1317.
[69] A.C. Leskovjan, A. Kretlow, L.M. Miller, Anal. Chem. 82 (2010) 2711–2716.
[70] J.H. Park, W. Sun, M. Cui, Proc. Natl. Acad. Sci. 112 (2015) 9236–9241.
[71] V.P.B. Grover, J.M. Tognarelli, M.M.E. Crossey, et al., J. Clin. Exp. Hepatol. 5 (2015) 246–255.
[72] T. Fernández, A. Martínez-Serrano, L. Cussó, M. Desco, M. Ramos-Gómez, ACS Chem. Neurosci. 9 (2018) 912–924.
[73] L. Chen, Z. Wei, K.W.Y. Chan, et al., Neuroimage 188 (2019) 380–390.
[74] J. Liu, C. Chen, H. Chen, et al., Anal. Chem. 94 (2022) 16213–16221.
[75] H. Takahashi, K. Ishii, N. Kashiwagi, et al., Clin. Radiol. 72 (2017) 108–115.
[76] T. Prasath, V. Sumathi, Int. J. Environ. Res. Public Health 20 (2023) 1273.
[77] M.B. Hulkower, D.B. Poliak, S.B. Rosenbaum, M.E. Zimmerman, M.L. Lipton, Am. J. Neuroradiol. 34 (2013) 2064–2074.
[78] N.A. Johnson, G.H. Jahng, M.W. Weiner, et al., Radiology 234 (2005) 851–859.
[79] H.Y.A. Mhanna, A.F. Omar, Y.M. Radzi, et al., Heliyon 11 (2025) e42464.
[80] V. Kotoula, J.W. Evans, C.E. Punturieri, C.A. Zarate, Front. Neuroimaging 2 (2023) 1110258.
[81] J.M. Soares, R. Magalhães, P.S. Moreira, et al., Front. Neurosci. 10 (2016) 515.
[82] P. Ren, M. Ma, G. Xie, Z. Wu, D. Wu, Aging 12 (2020) 13571–13582.
[83] C. Li, M. Liu, J. Xia, et al., IEEE J. Biomed. Health Inform. 27 (2023) 5430–5438.
[84] N. Falgàs, M. Peña-González, A. Val-Guardiola, et al., Alzheimer's Dement. 20 (2024) 6351–6364.
[85] S. Ruiz, S. Lee, S.R. Soekadar, et al., Hum. Brain Mapp. 34 (2013) 200–212.
[86] M. Mitolo, M. Stanzani-Maserati, S. Capellari, et al., Neuroimage Clin. 23 (2019) 101843.
[87] P. Chen, Z. Shen, Q. Wang, et al., Front. Aging Neurosci. 13 (2021) 618690.
[88] X. Xu, J. Xu, K.W.Y. Chan, et al., Magn. Reson. Med. 81 (2018) 47–56.
[89] L. Xu, L. Lai, Y. Wen, et al., ACS Chem. Neurosci. 14 (2023) 226–234.
[90] C.C. Yang, S.Y. Yang, J.J. Chieh, et al., ACS Chem. Neurosci. 2 (2011) 500–505.
[91] H. Skaat, S. Margel, Biochem. Biophys. Res. Commun. 386 (2009) 645–649.
[92] A.F. Martins, J.F. Morfin, A. Kubíčková, et al., ACS Med. Chem. Lett. 4 (2013) 436–440.
[93] Y. Lin, K. Huang, H. Xu, et al., Clin. Neurophysiol. 131 (2020) 2429–2439.
[94] A. Rubinski, N. Franzmeier, J. Neitzel, M. Ewers, Alzheimer's Res. Ther. 12 (2020) 133.
[95] J.L. Whitwell, J. Graff-Radford, N. Tosakulwong, et al., Alzheimer's, Dementia 14 (2018) 1005–1014.
[96] A. Touroutoglou, Y. Katsumi, M. Brickhouse, et al., Alzheimer's Dement. 19 (2023) S74–S88.
[97] D. Jin, B. Zhou, Y. Han, et al., Adv. Sci. 7 (2020) 2000675.
[98] A. Ortiz, J.M. Górriz, J. Ramírez, F.J. Martínez-Murcia, Pattern Recognit. Lett. 34 (2013) 1725–1733.
[99] Q. Zhang, J. Sheng, Q. Zhang, et al., Comput. Biol. Med. 165 (2023) 107392.
[100] G. Cao, M. Zhang, Y. Wang, et al., Comput. Biol. Med. 163 (2023) 107110.
[101] V. Sanjay, P. Swarnalatha, Alex. Eng. J. 104 (2024) 451–463.
[102] R. Sampath, M. Baskar, J. Prev, Alzheimer's Dis. 11 (2024) 1106–1121.
[103] X. Gao, H. Liu, F. Shi, D. Shen, M. Liu, IEEE J. Biomed. Health Inform. 27 (2023) 4961–4970.
[104] H. Cai, Q. Zhang, Y. Long, Comput. Biol. Med. 154 (2023) 106570.
[105] C.D. Mayo, M.A. Garcia-Barrera, E.L. Mazerolle, et al., Front. Aging Neurosci. 10 (2019) 436.

[106] N. Shu, Y. Liang, H. Li, J. Zhang, et al., Radiology 265 (2012) 518–527.
[107] H.K.F. Mak, W. Qian, K.S. Ng, et al., J. Alzheimer's Dis. 41 (2014) 749–758.
[108] E.T. Petersen, T. Lim, X. Golay, Magn. Reson. Med. 55 (2006) 219–232.
[109] M.I.S.S. Agnollitto, R.F. Leoni, M.P. Foss, et al., Dement. Neuropsychol. 25 (2023) e20230004.
[110] N. Zhang, M.L. Gordon, T.E. Goldberg, Neurosci. Biobehav. Rev. 72 (2017) 168–175.
[111] T. Dashjamts, T. Yoshiura, A. Hiwatashi, et al., Acad. Radiol. 18 (2011) 1492–1499.
[112] H.F. Kung, S.R. Choi, W. Qu, W. Zhang, D. Skovronsky, J. Med. Chem. 53 (2009) 933–941.
[113] K. Terpstra, Y. Wang, T.T. Huynh, et al., Inorg. Chem. 61 (2022) 20326–20336.
[114] M.V. Fawaz, A.F. Brooks, M.E. Rodnick, et al., ACS Chem. Neurosci. 5 (2014) 718–730.
[115] K. Matsumura, M. Ono, H. Kimura, et al., ACS Med. Chem. Lett. 3 (2011) 58–62.
[116] Y. Okumura, Y. Maya, T. Onishi, et al., ACS Chem. Neurosci. 9 (2018) 1503–1514.
[117] K. Serdons, C. Terwinghe, P. Vermaelen, et al., J. Med. Chem. 52 (2009) 1428–1437.
[118] T.J. Betthauser, K.A. Cody, M.D. Zammit, et al., J. Nucl. Med. 60 (2019) 93–99.
[119] S. Sanabria Bohórquez, J. Marik, A. Ogasawara, et al., Eur. J. Nucl. Med. Mol. Imaging 46 (2019) 2077–2089.
[120] N. Lazarova, S.S. Zoghbi, J. Hong, et al., J. Med. Chem. 51 (2008) 6034–6043.
[121] W. Zheng, Y. Huang, H. Chen, et al., ACS Chem. Neurosci. 14 (2023) 988–1003.
[122] A. Mueller, S. Bullich, O. Barret, et al., J. Nucl. Med. 61 (2020) 911–919.
[123] D.T. Chien, S. Bahri, A.K. Szardenings, et al., J. Alzheimer's Dis. 34 (2013) 457–468.
[124] A.S. Fleisher, M.J. Pontecorvo, M.D. Devous, et al., JAMA Neurol. 77 (2020) 829–839.
[125] J. Dronse, K. Fliessbach, G.N. Bischof, et al., J. Alzheimer's Dis. 55 (2016) 465–471.
[126] H. Kuwabara, R.A. Comley, E. Borroni, et al., J. Nucl. Med. 59 (2018) 1877–1884.
[127] M.S. Goyal, T. Blazey, N.V. Metcalf, et al., Proc. Natl. Acad. Sci. U. S. A. 120 (2023) e2212256120.
[128] A. Wabik, E. Trypka, J. Bladowska, et al., J. Transl. Med. 20 (2022) 259.
[129] X. Pan, M. Adel, C. Fossati, et al., Comput. Methods Programs Biomed. 180 (2019) 105027.
[130] D. Sehlin, X.T. Fang, L. Cato, et al., Nat. Commun. 7 (2016) 10759.
[131] S.R. Meier, S. Syvänen, G. Hultqvist, et al., J. Nucl. Med. 59 (2018) 1885–1891.
[132] S. Syvänen, J. Eriksson, ACS Chem. Neurosci. 4 (2012) 225–237.
[133] L.E. McInnes, A. Noor, K. Kysenius, et al., Inorg. Chem. 58 (2019) 3382–3395.
[134] N. Sheikh-Bahaei, S.A. Sajjadi, R. Manavaki, et al., Ann. Neurol. 83 (2018) 771–778.
[135] Z. Li, M. Cui, J. Dai, et al., J. Med. Chem. 56 (2013) 471–482.
[136] X. Zhang, P. Yu, Y. Yang, et al., Bioconjug. Chem. 27 (2016) 2493–2504.
[137] B. Spyrou, I.N. Hungnes, F. Mota, et al., Inorg. Chem. 60 (2021) 13669–13680.
[138] M. Sagnou, B. Mavroidi, A. Shegani, et al., J. Med. Chem. 62 (2019) 2638–2650.
[139] X. Zhang, Y. Hou, C. Peng, et al., J. Med. Chem. 61 (2018) 1330–1339.
[140] Y. Maya, M. Ono, H. Watanabe, et al., Bioconjug. Chem. 20 (2009) 95–101.
[141] E. Schlein, S. Syvänen, J. Rokka, et al., Mol. Biopharm. 19 (2022) 4111–4122.
[142] H. Watanabe, T. Kishimoto, S. Kaide, et al., ACS Med. Chem. Lett. 12 (2021) 805–811.
[143] M. Takahashi, T. Tada, T. Nakamura, K. Koyama, T. Momose, Am. J. Alzheimer's Dis. Other Dement. 34 (2019) 314–321.
[144] Y. Höller, A.C. Bathke, A. Uhl, et al., Front. Aging Neurosci. 9 (2017) 290.
[145] Y.C. Ni, F.P. Tseng, M.C. Pai, et al., Diagnostics 11 (2021) 2091.
[146] F.P.M. Oliveira, Z. Walker, R.W.H. Walker, et al., J. Neurol. Neurosurg. Psychiatry 92 (2021) 662–667.
[147] R. Ni, A. Villois, X.L. Dean-Ben, et al., Photoacoustics 23 (2021) 100285.
[148] S.S. Shin, T.A.G.M. Huisman, M. Hwang, J. Ultrasound Med. 37 (2018) 1857–1867.
[149] Y.J. Ho, C.C. Huang, C.H. Fan, et al., Cell. Mol. Life Sci. 78 (2021) 6119–6141.
[150] R. Liu, J. Tang, Y. Xu, Z. Dai, ACS Nano 13 (2019) 5124–5132.
[151] C. Morisset, A. Dizeux, B. Larrat, et al., Sci. Rep. 12 (2022) 19515.
[152] W. Wang, X. Wu, K.W. Kevin Tang, et al., J. Am. Chem. Soc. 145 (2023) 1097–1107.
[153] E.P. Hackett, B.R. Shah, B. Cheng, et al., ACS Chem. Neurosci. 12 (2021) 2820–2828.
[154] B. Ling, J. Lee, D. Maresca, et al., ACS Nano 14 (2020) 12210–12221.
[155] H. Huang, P.L. Hsu, S.F. Tsai, et al., Adv. Sci. 10 (2023) 2302345.
[156] H.C. Li, P.Y. Chen, H.F. Cheng, Y.M. Kuo, C.C. Huang, IEEE Trans. Biomed. Eng. 66 (2019) 3393–3401.
[157] S. Wang, Z. Li, Y. Liu, et al., Sens. Actuators B 267 (2018) 403–411.
[158] H. Li, P. Zhang, L.P. Smaga, R.A. Hoffman, J. Chan, J. Am. Chem. Soc. 137 (2015) 15628–15631.
[159] J. Zhang, X. Zhen, P.K. Upputuri, et al., Adv. Mater. 29 (2017) 1604764.
[160] S. Wang, G. Yu, Y. Ma, et al., ACS Appl. Mater. Interfaces 11 (2018) 1917–1923.
[161] Y. Han, H. Yi, Y. Wang, et al., ACS Nano 16 (2022) 19053–19066.
[162] Z. Jiang, Z. Liang, Y. Cui, et al., J. Am. Chem. Soc. 145 (2023) 7952–7961.
[163] T. Guo, K. Xiong, B. Yuan, et al., Photoacoustics 31 (2023) 100516.
[164] S. Wang, Z. Sheng, Z. Yang, et al., Angew. Chem. Int. Ed. 58 (2019) 12415–12419.
[165] S. Na, J.J. Russin, L. Lin, et al., Nat. Biomed. Eng. 6 (2022) 584–592.
[166] X. Wang, Y. Pang, G. Ku, et al., Nat. Biotechnol. 21 (2003) 803.
[167] R.P.Y. Chen, M.G. Soliman, H.A. Davies, et al., PLoS ONE 17 (2022) e0259608.
[168] D. Razansky, J. Klohs, R. Ni, Eur. J. Nucl. Med. Mol. Imaging 48 (2021) 4152–4170.
[169] P. Vagenknecht, A. Luzgin, M. Ono, et al., Eur. J. Nucl. Med. Mol. Imaging 49 (2022) 2137–2152.
[170] S. Jo, I.C. Sun, C.H. Ahn, S. Lee, K. Kim, ACS Appl. Mater. Interfaces 15 (2022) 120–137.
[171] C. Li, G. Chen, Y. Zhang, F. Wu, Q. Wang, J. Am. Chem. Soc. 142 (2020) 14789–14804.
[172] S. Wang, H. Shi, L. Wang, et al., J. Am. Chem. Soc. 144 (2022) 23668–23676.
[173] Z. Sheng, B. Guo, D. Hu, et al., Adv. Mater. 30 (2018) 1800766.
[174] M. Cui, M. Ono, H. Watanabe, et al., J. Am. Chem. Soc. 136 (2014) 3388–3394.
[175] Y. Ge, F. Zeng, G. Sun, et al., ACS Chem. Neurosci. 12 (2021) 3683–3689.
[176] K. Zhou, Y. Li, Y. Peng, et al., Anal. Chem. 90 (2018) 8576–8582.
[177] C. Li, L. Cao, Y. Zhang, et al., Small 11 (2015) 4517.
[178] H.L. Yang, S.Q. Fang, Y.W. Tang, et al., Eur. J. Med. Chem. 179 (2019) 736–743.
[179] F. Chibhabha, Y. Yang, K. Ying, et al., J. Mater. Chem. B 8 (2020) 7438–7452.
[180] L. Quan, J. Wu, L.A. Lane, et al., Bioconjug. Chem. 27 (2016) 809–814.
[181] K. Liu, T.L. Guo, J. Chojnacki, et al., ACS Chem. Neurosci. 3 (2012) 141–146.
[182] S.C. Lee, H.H. Park, S.H. Kim, et al., Anal. Chem. 91 (2019) 5573–5581.
[183] W. Gao, W. Wang, X. Dong, Y. Sun, Small 16 (2020) e2002804.
[184] A.A. Elbatrawy, S.J. Hyeon, N. Yue, et al., ACS Sens. 6 (2021) 2281–2289.
[185] Y. Seo, K.S. Park, T. Ha, et al., ACS Chem. Neurosci. 7 (2016) 1474–1481.
[186] Z. He, D. Liu, Y. Liu, et al., Anal. Chem. 94 (2022) 10256–10262.
[187] D. Huang, Q. Wang, Y. Cao, et al., ACS Nano 17 (2023) 5033–5046.
[188] H. Li, J. Wang, Y. Li, et al., Sens. Actuators B 358 (2022) 131481.
[189] L. Streich, C. Boffi, J.L. Wang, et al., Nat. Methods 18 (2021) 1253–1258.
[190] C. Chen, Z. Liang, B. Zhou, et al., ACS Chem. Neurosci. 9 (2018) 3128–3136.
[191] X. Xie, G. Liu, Y. Niu, et al., Anal. Chem. 93 (2021) 15088–15095.
[192] D. Kim, S.H. Baik, S. Kang, et al., ACS Cent. Sci. 2 (2016) 967–975.
[193] J. Yang, B. Zhu, W. Yin, et al., Chem. Sci. 11 (2020) 5238–5245.
[194] X. Xie, Y. Liu, G. Liu, et al., Chem. Commun. 58 (2022) 6300–6303.
[195] X. Wang, Y. Liu, X. Wang, et al., Biosens. Bioelectron. 238 (2023) 115563.
[196] Z. Gong, Z. Liu, Z. Zhang, Y. Mei, Y. Tian, CCS Chem. 4 (2022) 2020–2030.
[197] O. Babourina, Z. Rengel, Methods Mol. Biol. 913 (2012) 149–161.
[198] L. Ge, Y. Tian, Anal. Chem. 91 (2019) 3294–3301.
[199] D.E.S. Silva, M.P. Cali, W.M. Pazin, et al., J. Med. Chem. 59 (2016) 9215–9227.
[200] Y. Liu, S. Walter, M. Stagi, et al., Brain 128 (2005) 1778–1789.
[201] Z. Wu, M. Liu, Z. Liu, Y. Tian, J. Am. Chem. Soc. 142 (2020) 7532–7541.
[202] K.V. Kuchibhotla, C.R. Lattarulo, B.T. Hyman, B.J. Bacskai, Science 323 (2009) 1211–1215.
[203] N. Xia, B. Zhou, N. Huang, et al., Biosens. Bioelectron. 85 (2016) 625–632.
[204] F.O. Talbot, A. Rullo, H. Yao, R.A. Jockusch, J. Am. Chem. Soc. 132 (2010) 16156–16164.
[205] X.H. Wen, X.F. Zhao, X.H. Wang, et al., ACS Appl. Nano Mater. 5 (2022) 15925–15933.
[206] W.K. Fang, L. Liu, L.L. Zhang, et al., Anal. Chem. 93 (2021) 12447–12455.
[207] Q. Zhang, B. Yin, Y. Huang, et al., Biosens. Bioelectron. 230 (2023) 115270.
[208] S. Lee, E. Kim, C.E. Moon, et al., Nat. Commun. 14 (2023) 8153.
[209] X.P. He, Q. Deng, L. Cai, et al., ACS Appl. Mater. Interfaces 6 (2014) 5379–5382.
[210] S.A. James, Q.I. Churches, M.D. de Jonge, ACS Chem. Neurosci. 8 (2016) 629–637.
[211] S. Zha, H. Liu, H. Li, et al., ACS Nano 18 (2024) 1820–1845.
[212] N. Gustavsson, A. Paulus, I. Martinsson, et al., Light Sci. Appl. 10 (2021) 151.
[213] N. Fimognari, A. Hollings, V. Lam, et al., ACS Chem. Neurosci. 9 (2018) 2774–2785.
[214] L.G. Rodriguez, S.J. Lockett, G.R. Holtom, Cytom. Part A 69A (2006) 779–791.
[215] D. Polli, V. Kumar, C.M. Valensise, M. Marangoni, G. Cerullo, Laser Photonics Rev. 12 (2018) 1800020.
[216] I. Kaya, D. Brinet, W. Michno, et al., ACS Chem. Neurosci. 8 (2017) 347–355.
[217] I. Kaya, H. Zetterberg, K. Blennow, J. Hanrieder, ACS Chem. Neurosci. 9 (2018) 1802–1817.
[218] C. Zhu, J. Han, F. Liang, et al., Coord. Chem. Rev. 517 (2024) 216002.
[219] J.P.R. Day, K.F. Domke, G. Rago, et al., J. Phys. Chem. B 115 (2011) 7713–7725.
[220] I. Uras, M. Karayel-Basar, B. Sahin, A.T. Baykal, Alzheimer's Dement. 19 (2023) 4572–4589.
[221] L. Carlred, A. Gunnarsson, S. Solé-Domènech, J. Am. Chem. Soc. 136 (2014) 9973–9981.
[222] Y. Chen, C. Xie, X. Wang, et al., Anal. Chem. 94 (2022) 15367–15376.
[223] T.R. Hawkinson, H.A. Clarke, L.E.A. Young, Alzheimer's Dement. 18 (2022) 1721–1735.
[224] Q. Zhang, Y. Li, P. Sui, et al., Talanta 266 (2024) 125022.
[225] N. Kakuda, T. Miyasaka, N. Iwasaki, Acta Neuropathol. Commun. 5 (2017) 73.
[226] E. Llanos-González, F.J. Sancho-Bielsa, J. Frontiñán-Rubio, et al., Antioxidants 12 (2023) 747.
[227] D.W. Moon, Y.H. Park, S.Y. Lee, et al., ACS Appl. Mater. Interfaces 12 (2020) 18056–18064.
[228] K. Dimovska Nilsson, A. Karagianni, I. Kaya, M. Henricsson, J.S. Fletcher, Anal. Bioanal. Chem. 413 (2021) 4181–4194.
[229] A.N. Lazar, C. Bich, M. Panchal, et al., Acta Neuropathol. 125 (2012) 133–144.
[230] R.W. Hutchinson, A.G. Cox, C.W. McLeod, et al., Anal. Biochem. 346 (2005) 225–233.
[231] X. Zhang, C. Wu, W. Tan, J. Proteome Res. 20 (2021) 2643–2650.
[232] H. Zhang, F. Shi, Y. Yan, C. Deng, N. Sun, Adv. Healthc. Mater. 12 (2023) 2301136.
[233] Y. Li, S.E. Schindler, J.G. Bollinger, et al., Neurology 98 (2022) e688–e699.

[234] C. Hirtz, G.U. Busto, K. Bennys, et al., Alzheimer's Res. Ther. 15 (2023) 34.
[235] R. Haque, C.M. Watson, J. Liu, et al., Sci. Transl. Med. 15 (2023) eadg4122.
[236] T. West, K.M. Kirmess, M.R. Meyer, et al., Mol. Neurodegener. 16 (2021) 30.
[237] N.R. Barthélemy, G. Salvadó, S.E. Schindler, et al., Nat. Med. 30 (2024) 1085–1095.
[238] W. Le, G. Xu, S. Li, et al., Aging Dis. 11 (2020) 1459–1470.
[239] Y. Garini, I.T. Young, G. McNamara, Cytom. Part A 69A (2006) 735–747.
[240] M. Ji, M. Arbel, L. Zhang, et al., Sci. Adv. 4 (2018) eaat7715.
[241] K. Alkhuder, Photodiagn. Photodyn. Ther. 42 (2023) 103606.
[242] L. Huang, R. Luo, X. Liu, X. Hao, Light Sci. Appl. 11 (2022) 61.
[243] L.M. Miller, M.W. Bourassa, R.J. Smith, Biochim. Biophys. Acta Biomembr. 1828 (2013) 2339–2346.
[244] N. Benseny-Cases, O. Klementieva, M. Cotte, I. Ferrer, J. Cladera, Anal. Chem. 86 (2014) 12047–12054.
[245] F. Palombo, F. Tamagnini, J.C.G. Jeynes, et al., Analyst 143 (2018) 850–857.
[246] M.P. Confer, B.M. Holcombe, A.G. Foes, et al., J. Phys. Chem. Lett. 12 (2021) 9662–9671.
[247] G. Devitt, K. Howard, A. Mudher, S. Mahajan, ACS Chem. Neurosci. 9 (2018) 404–420.
[248] N. Kornienko, J. Resasco, N. Becknell, et al., J. Am. Chem. Soc. 137 (2015) 7448–7455.
[249] A. Folick, W. Min, M.C. Wang, Curr. Opin. Genet. Dev. 21 (2011) 585–590.
[250] S.S. Sinha, S. Jones, A. Pramanik, P.C. Ray, Acc. Chem. Res. 49 (2016) 2725–2735.
[251] J. Tittel, F. Knechtel, E. Ploetz, Adv. Funct. Mater. 34 (2024) 2307518.
[252] H.J. Park, S. Cho, M. Kim, Y.S. Jung, Nano Lett. 20 (2020) 2576–2584.
[253] J.K. Yang, I.J. Hwang, M.G. Cha, et al., Small 15 (2019) 1900613.
[254] Y. Zhou, J. Liu, T. Zheng, Y. Tian, Anal. Chem. 92 (2020) 5910–5920.
[255] X. Liu, X. Su, M. Chen, Y. Xie, M. Li, Biosens. Bioelectron. 245 (2024) 115840.
[256] Q. Xu, W. Liu, L. Li, et al., Chem. Commun. 53 (2017) 1880–1883.
[257] M. Sunder, N. Acharya, S. Nayak, N. Mazumder, Appl. Spectrosc. Rev. 56 (2020) 764–803.
[258] S. Li, Z. Luo, R. Zhang, et al., Biosensors 11 (2021) 365.
[259] D. Fu, W. Yang, X.S. Xie, J. Am. Chem. Soc. 139 (2016) 583–586.
[260] R.R. Jones, D.C. Hooper, L. Zhang, D. Wolverson, V.K. Valev, Nanoscale Res. Lett. 14 (2019) 231.
[261] C.H.Jr. Camp, Y.J. Lee, J.M. Heddleston, et al., Nat. Photonics 8 (2014) 627–634.
[262] N.K. Mahanti, R. Pandiselvam, A. Kothakota, et al., Trends Food Sci. Technol. 120 (2022) 418–438.
[263] X. Hadoux, F. Hui, J.K.H. Lim, et al., Nat. Commun. 10 (2019) 4227.
[264] M. Vandenabeele, L. Veys, S. Lemmens, et al., Acta Neuropathol. Commun. 9 (2021) 6.
[265] S.S. More, J.M. Beach, C. McClelland, A. Mokhtarzadeh, R. Vince, ACS Chem. Neurosci. 10 (2019) 4492–4501.
[266] X. Du, Y. Koronyo, N. Mirzaei, et al., PNAS Nexus 1 (2022) pgac164.
[267] S.S. More, J.M. Beach, R. Vince, Investig. Ophthalmol. Vis. Sci. 57 (2016) 3231–3238.
[268] L.E. Jennings, N.J. Long, Chem. Commun. 24 (2009) 3511–3524.
[269] P.M. Wehrli, J. Ge, W. Michno, et al., JACS Au 3 (2023) 762–774.
[270] C.N. Jiao, Y.L. Gao, D.H. Ge, Eng. Appl. Artif. Intell. 130 (2024) 107782.
[271] W. Lin, W. Lin, G. Chen, et al., Front. Neurosci. 15 (2021) 646013.
[272] F. Liu, C.Y. Wee, H. Chen, D. Shen, Neuroimage 84 (2014) 466–475.
[273] J. Cheng, H. Wang, S. Wei, et al., Comput. Biol. Med. 170 (2024) 108000.
[274] R. Camedda, C.G. Bonomi, M.G. Di Donna, A. Chiaravalloti, Int. J. Mol. Sci. 24 (2023) 751.
[275] X. Wang, H.N. Chan, N. Desbois, et al., ACS Appl. Mater. Interfaces 13 (2021) 18525–18532.
[276] J.H. Jhoo, D.Y. Lee, I.H. Choo, et al., Psychiatry Res. Neuroimaging 183 (2010) 237–243.
[277] K.B. Walhovd, A.M. Fjell, I. Amlien, et al., Neuroimage 45 (2009) 215–223.
[278] L. Lai, X. Jiang, S. Han, et al., Langmuir 33 (2017) 9018–9024.
[279] M. Maruyama, H. Shimada, T. Suhara, et al., Neuron 79 (2013) 1094–1108.
[280] W. Michno, I. Kaya, S. Nyström, et al., Anal. Chem. 90 (2018) 8130–8138.
[281] I. Kaya, D. Brinet, W. Michno, et al., ACS Chem. Neurosci. 8 (2017) 2778–2790.
[282] J. Ge, S. Koutarapu, D. Jha, et al., Anal. Chem. 95 (2023) 4692–4702.
[283] N. Hao, Z. Wang, P. Liu, et al., Biosens. Bioelectron. 196 (2022) 113730.
[284] J.H. Lee, D.H. Kim, W.K. Song, M.K. Oh, D.K. Ko, Biomed. Opt. 20 (2015) 056013.
[285] K.L. Summers, N. Fimognari, A. Hollings, et al., Biochemistry 56 (2017) 4107–4116.
[286] M. Zangiabadi, A. Ghosh, Y. Zhao, ACS Nano 17 (2023) 4764–4774.
[287] X. Wang, D. Niu, P. Li, et al., ACS Nano 96 (2015) 5646–5656.
[288] Z. Luo, H. Xu, S. Samanta, et al., Biomedicines 10 (2022) 2949.
[289] S. Lemmens, T. Van Craenendonck, J. Van Eijgen, et al., Alzheimer's Res. Ther. 12 (2020) 144.
[290] C.I.P. Chaparro, B.T. Simões, J.P. Borges, et al., Pharmaceutics 15 (2023) 2316.
[291] Y. Jiang, W. Li, Y. Ma, Y. Hou, J. Mater. Chem. B 13 (2025) 1424–1436.
[292] F. Morales-Zavala, P. Jara-Guajardo, D. Chamorro, et al., Biomater. Sci. 9 (2021) 4178–4190.
[293] G. Agraharam, N. Saravanan, A. Girigoswami, K. Girigoswami, BioNanoScience 12 (2022) 1002–1007.
[294] N. Song, S. Sun, K. Chen, et al., J. Control. Release 360 (2023) 392–417.
[295] A. Panghal, S.J.S. Flora, Biochim. Biophys. Acta Gen. Subj. 1868 (2024) 130559.
[296] X. Dai, Y. Li, Y. Zhong, Glob. J. Nano 4 (2018) 555644.
[297] L. Li, R. He, H. Yan, et al., Nano Today 47 (2022) 101654.
[298] C.L. Evans, X.S. Xie, Annu. Rev. Anal. Chem. 1 (2008) 883–909.
[299] C.H. Camp Jr, M.T. Cicerone, Nat. Photonics 9 (2015) 295–305.
[300] J. Sun, L. Li, W. Cai, A. Chen, R. Zhang, ACS Appl. Bio Mater. 4 (2021) 5312–5323.
[301] R. Chakravarty, H. Hong, W. Cai, Mol. Pharm. 11 (2014) 3777–3797.
[302] S.T.G. Bruijnen, D.M.S.H. Chandrupatla, L. Giovanonni, et al., Mol. Pharm. 16 (2018) 273–281.
[303] J. Ahlawat, G. Guillama Barroso, S. Masoudi Asil, et al., ACS Omega 5 (2020) 12583–12595.
[304] N. Lipsman, Y. Meng, A.J. Bethune, et al., Nat. Commun. 9 (2018) 2336.
[305] A. Burgess, S. Dubey, S. Yeung, et al., Radiology 273 (2014) 736–745.
[306] A.R. Rezai, M. Ranjan, P.F. D'Haese, et al., Proc. Natl. Acad. Sci. U. S. A. 117 (2020) 9180–9182.
[307] K. Xhima, K. Markham-Coultes, H. Nedev, et al., Sci. Adv. 6 (2020) eaax6646.
[308] R.M. Nisbet, A. Van der Jeugd, G. Leinenga, et al., Brain 140 (2017) 1220–1230.
[309] A.I. Bush, S.B. Raymond, L.H. Treat, et al., PLoS One 3 (2008) e2175.
[310] J. Zhao, F. Yin, L. Ji, et al., ACS Appl. Mater. Interfaces 12 (2020) 44447–44458.
[311] R. Beisteiner, E. Matt, C. Fan, et al., Adv. Sci. 23 (2019) 1902583.
[312] J. Wang, P. Shangguan, X. Chen, et al., Nat. Commun. 15 (2024) 705.
[313] M. Sharma, V. Tiwari, S. Chaturvedi, et al., ACS Appl. Mater. Interfaces 14 (2022) 13079–13093.
[314] K. Qian, X. Bao, Y. Li, et al., ACS Nano 16 (2022) 11455–11472.
[315] I. Ahmad, A. Mozhi, L. Yang, et al., Colloids Surf. B 159 (2017) 540–545.
[316] D. Liu, B. Lin, W. Shao, et al., ACS Appl. Mater. Interfaces 6 (2014) 2131–2136.
[317] T. Li, C. Li, Z. Ruan, et al., ACS Nano 13 (2019) 3691–3702.
[318] Y. Liu, Y. Chen, Y. Gong, H. Yang, J. Liu, ACS Appl. Nano Mater. 6 (2023) 5384–5393.
[319] K. Ge, Y. Mu, M. Liu, et al., ACS Appl. Mater. Interfaces 14 (2022) 3662–3674.
[320] T. Yin, W. Xie, J. Sun, L. Yang, J. Liu, ACS Appl. Mater. Interfaces 8 (2016) 19291–19302.
[321] M. Li, X. Yang, J. Ren, K. Qu, X. Qu, Adv. Mater. 24 (2012) 1722–1728.
[322] E.N. Musa, K.C. Stylianou, Mol. Syst. Des. Eng. 8 (2023) 151–166.
[323] Z.W. Tay, P. Chandrasekharan, A. Chiu-Lam, et al., ACS Nano 12 (2018) 3699–3713.
[324] J.H. Yan, W. Meng, H. Shan, et al., ACS Appl. Nano Mater. 4 (2021) 1351–1363.
[325] A. Detappe, E. Thomas, M.W. Tibbitt, et al., Nano Lett. 17 (2017) 1733–1740.
[326] N. Dong, P. Ali-Khiavi, N. Ghavamikia, et al., Neurol. Sci. 46 (2025) 1489–1507.
[327] Q. Song, J. Li, T. Li, H.W. Li, Adv. Sci. 11 (2024) 2403473.
[328] U. Aziz, H.G. Nigel, A.K. Mohammad, Curr. Med. Chem. 30 (2023) 255–270.
[329] M. Bilal, M. Barani, F. Sabir, A. Rahdar, G.Z. Kyzas, NanoImpact 20 (2020) 100251.
[330] M.E. Wechsler, J.E. Vela Ramirez, N.A. Peppas, Ind. Eng. Chem. Res. 58 (2019) 15079–15087.
[331] E. Asimakidou, J.K.S. Tan, J. Zeng, C.H. Lo, Pharmaceuticals 17 (2024) 612.
[332] M.T. Khosroshahi, S. Morsali, S. Gharakhanlou, et al., Diagnostics 15 (2025) 612.
[333] I. Malik, A. Iqbal, Y.H. Gu, M.A. Al-Antari, Diagnostics 14 (2024) 1281.
[334] K. Fujita, M. Katsuki, A. Takasu, et al., Aging Med. 5 (2022) 167–173.
[335] J.R. Teoh, J. Dong, X. Zuo, et al., PeerJ Comput. Sci. 10 (2024) e2298.
[336] X. Zhao, C.K.E. Ang, U.R. Acharya, K.H. Cheong, Biocybern. Biomed. Eng. 41 (2021) 456–473.
[337] M.O. Etekochay, A.R. Amaravadhi, G.V. González, et al., J. Alzheimer's Dis. 99 (2024) 1–20 https://journals.sagepub.com/doi/10.3233/JAD-231135.
[338] H. Ashayeri, A. Jafarizadeh, M. Yousefi, et al., Clin. Exp. Ophthalmol. 262 (2024) 2389–2401.